



Characterization of hollow cathode plasma turbulence using coherent Thomson scattering

S. Tsikata, K. Hara, S. Mazouffre

► To cite this version:

S. Tsikata, K. Hara, S. Mazouffre. Characterization of hollow cathode plasma turbulence using coherent Thomson scattering. *Journal of Applied Physics*, 2021, 130 (24), pp.243304. 10.1063/5.0071650 . hal-03536541

HAL Id: hal-03536541

<https://hal.science/hal-03536541v1>

Submitted on 26 Nov 2022

HAL is a multi-disciplinary open access archive for the deposit and dissemination of scientific research documents, whether they are published or not. The documents may come from teaching and research institutions in France or abroad, or from public or private research centers.

L'archive ouverte pluridisciplinaire **HAL**, est destinée au dépôt et à la diffusion de documents scientifiques de niveau recherche, publiés ou non, émanant des établissements d'enseignement et de recherche français ou étrangers, des laboratoires publics ou privés.

Characterization of hollow cathode plasma turbulence using coherent Thomson scattering

S. Tsikata,¹ K. Hara,² and S. Mazouffre¹

¹⁾*Centre National de la Recherche Scientifique (CNRS), ICARE UPR 3021, 45071 Orléans, France*

²⁾*Department of Aeronautics and Astronautics, Stanford University, Stanford, 94305 CA, USA*

(*Electronic mail: sedina.tsikata@cnrs-orleans.fr)

(Dated: 17 November 2021)

Turbulence in hollow cathodes used for space propulsion is believed to play an important role in anomalous electron transport and ion heating. In this work, the implementation of coherent Thomson scattering to identify and characterize MHz-frequency ion acoustic turbulence and kHz-frequency oscillations in the plume of a hollow cathode is achieved. In the presence of a background magnetic field of a Hall thruster, a number of unstable modes are observed. A directive ion acoustic mode propagating predominantly within a restricted angle around the magnetic field is found, exhibiting an energy scaling with wavenumber k of the form $k^{-5.2 \pm 0.58}$, which differs from the classic Kadomtsev k^{-3} scaling for unmagnetized conditions. Bi-directional ion acoustic mode fluctuations propagating over a range of angles with respect to the magnetic field have been measured, possibly signifying the existence of a large-amplitude plasma wave, similar to the Buneman instability. Lastly, electron density fluctuations in the kHz-frequency range, a possible consequence of drift-driven instabilities in the plane perpendicular to the magnetic field, have also been identified. These results not only are an indication of the diversity of wave types which exist in hollow cathode plumes but also point to the key role played by the presence of, and the configuration of, the magnetic field in their appearance.

I. INTRODUCTION

Hollow cathodes, in which thermionic emission is used to produce an electron stream, have been a topic of active research for several years. They are critical components of electric propulsion systems, acting as a source of electrons to seed and maintain the plasma discharge, and as neutralizers for the accelerated ion beams generated in such devices. Recent extensive topical reviews^{1,2} on hollow cathodes, and the references cited therein, detail the breadth of studies which have been undertaken on their characteristic regimes, mode transitions, design, optimization and modeling over decades.

There has been increased investment in electric propulsion technologies³ in recent decades, with high-power (kilowatt-range) thrusters being of particular interest for scientific and potentially manned missions, while low-power devices (tens to hundreds of watts) are key to the expanding micro- and nano-satellite market⁴. Leading electric propulsion technologies, such as Hall effect thrusters and gridded ion thrusters, require reliable, adequately-scaled cathodes whose performance can be predicted by suitable numerical models. At present, there are still complex features of cathodes yet to be fully revealed and understood, such as the presence and impact of kinetic and fluid instabilities, and the exact nature of the coupling of the cathode plume to the main thruster plume. Several studies, such as Refs. 5–7, illustrate the role of cathode-thruster coupling in dictating discharge features, with improvements in characteristics such as beam divergence and efficiency observed when cathodes are centrally-mounted, compared to conventional externally-mounted configurations (still used in most propulsion systems, and the subject of the current work).

In this work, new experimental investigations are carried out using coherent Thomson scattering to identify unsta-

ble modes in hollow cathodes, taking advantage of the non-invasive nature of the diagnostic as well as the unique access it gives to electron density fluctuation measurements resolved in both angle and wavenumber. A particular focus is given to the identification and characterization of ion acoustic turbulence (IAT), which is driven naturally by the relative streaming of electrons and ions in the cathode plasma. Ion acoustic turbulence has been studied for decades as a driver of anomalous electron transport and ion heating, most notably in the context of shocks^{8,9}, with a number of theories developed to understand these effects^{10–13}.

Investigations of IAT in hollow cathodes have been carried out in several studies, where this mode was first invoked to account for higher-than-expected electron heating¹⁴ in the cathode plume. New and extensive information on its features and the conditions under which it arises have been gained from significant probe and analytical studies^{15–18}, along with evidence for its possible role in ion heating and its connection to hydrodynamic modes^{19–21}. In order to accurately model devices used in electric propulsion, there is a need for computational models that account for phenomena arising in both thrusters and cathodes, and greater understanding regarding how these plasmas couple²².

In recent years, coherent Thomson scattering has been applied to studies in electric propulsion to reveal the presence and features of kinetic modes such as the electron cyclotron drift instability^{23,24} and ion-ion two stream instability²⁵. In those applications, the non-invasive study of MHz-frequency, submillimeter-scale electron density fluctuations was used to measure dispersion relations, the angular extent of instability propagation, and propagation direction. These experimental studies have been directly motivated by numerical simulations²⁶ and have, in turn, driven new simulation efforts which have provided further insight into aspects such as nonlinear

mode coupling²⁷.

The application of this experimental technique to the study of hollow cathodes aims to provide detailed characterizations of instabilities such as ion acoustic modes. The ion acoustic mode attracted attention in the 1970s as a potential contributor to transport in shocks (either indirectly, coupled to Bernstein waves²⁸, or on its own²⁹) and was the subject of early coherent Thomson scattering investigations in work by authors such as Perratt *et al.*³⁰, Slusher and Surko³¹ and Pots *et al.*³². In this study, coherent Thomson scattering is now applied to identify and study IAT in cathodes currently relevant to electric propulsion.

This study seeks to identify instabilities and oscillations in a wide range of frequencies (kHz to MHz) in the vicinity of the hollow cathode during operation of a Hall thruster. Recent work from Hall and colleagues³³, using a standalone cathode and an external segmented anode designed to simulate a thruster magnetic field, shows that the presence of an applied magnetic field plays an important role in determining the features of the cathode plasma, including shape, oscillatory behavior, and operating mode. The anode configuration and location used in standalone operation also influence the cathode plasma features^{34,35}. Operation with a Hall thruster, in our study, provides a means of studying the development of cathode instabilities under standard conditions with a coupled thruster and cathode.

This manuscript is organized as follows. The experimental configuration implemented is described in Section II and the results obtained for the modes identified are presented and discussed in detail in Section III. Further discussion of the implications of this work are given in Section IV. A summary of the main conclusions is made in Section V.

II. EXPERIMENTAL IMPLEMENTATION

A. Hollow cathode

The hollow cathode used in this study is an orificed 5 A-class lanthanum hexaboride (LaB_6) model, mounted as shown in Fig. 1. It is to be noted that this cathode uses a pellet emitter (the violet rectangle in Fig. 1(a)), a difference with respect to hollow cathodes with tubular emitters³⁶. The LaB_6 pellet has a low work function and, when heated with a filament, emits electrons. Xenon is introduced into the cathode tube and ionized. A positive bias applied to the external cathode body allows it to act as a “keeper” to extract electrons and initiate the discharge. In the configuration shown in Fig. 1, the discharge is maintained by the flow of the electrons to the external thruster anode.

In this work, the cathode is operated in continuous heating mode (200 W) and with a 200 W Hall thruster. The thruster magnetic field (directed radially inwards) is generated by permanent magnets and has a magnitude of 250 G at the center of the channel axis at the exit plane. The cathode orifice is located at an axial distance of 12.9 mm from the thruster exit plane and 29.5 mm vertically below the center of the lower thruster channel, as depicted in Fig. 1. The measured

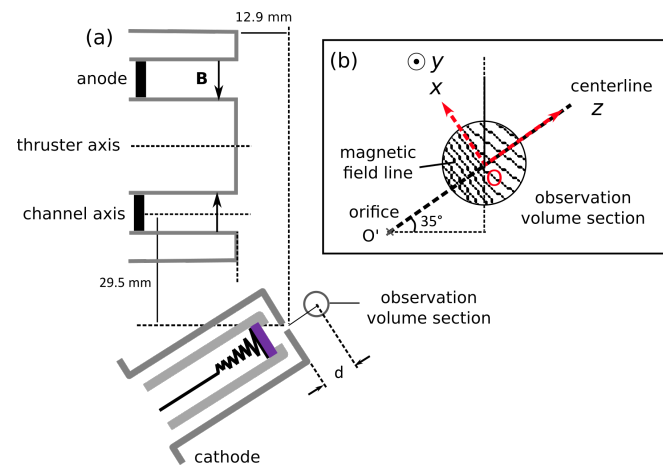


FIG. 1: Configuration of the cathode and Hall effect thruster in these investigations. In (a), the cross-section of the observation volume is indicated by a circle located a distance d from the cathode orifice. In (b), a magnified view of the observation volume section overlaid with the magnetic field lines within the section is shown. The (x, y, z) coordinate system is defined with respect to the center O of the observation volume, with z pointing along the cathode centerline. The angle between the cathode centerline and the thruster axis is 35° . Magnetic field lines in (b) show that alignment along z in experiments involves observation of fluctuations perpendicular to the centerline and within a 16° angular opening with respect to this perpendicular direction. The incoming laser beams point along y .

magnetic field at the cathode orifice is 25 G. Figure 1(a) also shows the cross-section of the scattering observation volume, located a distance d from the cathode orifice measured along the cathode centerline.

The present study focuses on fluctuations originating from the cathode plasma. In Fig. 1(b), a magnified view of the observation volume section is shown, overlaid with the magnetic field lines present in this section due to the cathode's proximity to the thruster. The field configuration in the section shown has been determined using Finite Element Method Magnetics (FEMM) modeling³⁷ of the thruster magnetic field. A coordinate system is defined with respect to the observation volume center O , where z points along the cathode centerline and axes perpendicular to the centerline are denoted as x and y . The angle between the cathode centerline and the thruster axis is 35° .

Magnetic field lines traversing the observation volume can be seen in Fig. 1(b) to be oriented mainly perpendicular to the cathode centerline. However, a more precise determination of the magnetic field line inclination with respect to the centerline shows that the inclination varies from 90° (magnetic field purely perpendicular to centerline) to 74° . Based on this angular opening of the magnetic field, when orienting the observation wave vector in the xOz plane to measure fluctuations, it is possible to recover fluctuations perpendicular to the centerline and fluctuations within, at most, a 16° deviation from the perpendicular direction.

An important difference between our configuration, which applies to conventional thruster assemblies with externally-mounted cathodes, and those of several other cathode studies, is worth mentioning. The Hall parameter at the position of the measurement volume is $\mathcal{O}(10 - 10^2)$, based on (i) an estimated value of the electron-neutral collision frequency³⁸ which assumes a neutral density of $10^{19} - 10^{20} \text{ m}^{-3}$, and (ii) an electron cyclotron frequency determined using a local magnetic field of 25 G. The electrons are strongly magnetized and in the observation volume, are directed along Ox on exiting the orifice. A multidimensional plasma simulation or other plasma diagnostics are required to understand the detailed plasma features, including the electric field structure, i.e., whether the field is predominantly aligned with, or perpendicular to, the magnetic field lines. We note that a finite electric field directed along Oz can initiate a wave propagating in the yOz plane.

In the majority of recent hollow cathode studies investigating instabilities, the cathode is operated either in the absence of a magnetic field, (as in Refs. 14,15,18) or with a magnetic field applied along the cathode axis (as in Refs. 33,39–42), and thus parallel to the electric field. The latter configuration is particularly relevant to high-power thrusters operated with centrally-mounted cathodes, but may be expected to give rise to instabilities with different features from those examined in the present study. As the use of externally-mounted hollow cathodes remains widespread, investigations of instabilities arising in these conventional configurations remain relevant.

B. Diagnostic and scattering configuration

This study uses a coherent Thomson scattering (CTS) diagnostic, PRAXIS, developed for the investigation of microturbulence²³ and based on the scattering of electromagnetic radiation on free charges (electrons). In the incoherent regime, scattered light is measured at length scales below the electron Debye length (λ_{De}), giving access to spectra reflecting uncorrelated electron motion. From such spectra, information regarding the electron temperature (more generally, electron energy distribution functions), density and drift velocity may be recovered⁴³. In contrast, the coherent (or alternatively, collective) Thomson regime used in these studies concerns measurements of scattered radiation at length scales greater than the electron Debye length. As such, these spectra are a reflection of correlated electron motion, which arises when a wave is present in the plasma. The detection of the plasma waves driven by instabilities is therefore possible via the observation of electron density fluctuations at the length scales of the wave activity, in a non-intrusive manner.

Thomson scattering techniques (incoherent and coherent) are well-established methods for non-invasive study of plasmas⁴⁴. The key challenge in implementing Thomson scattering in laboratory devices arises due to the low electron densities often encountered in such environments, down to 10^{16} m^{-3} (thus requiring diagnostics optimized for high sensitivity). In tokamaks, CTS has served as an important diagnostic for characterizing the contribution of microturbulence

to the anomalous electron diffusivity^{45–47} and in the development of scaling laws⁴⁸ for the plasma confinement time. The application of CTS to studies of laboratory plasmas, such as plasma columns and arcs^{31,32,49}, has been instrumental in the characterization of instabilities and effects such as mode damping.

For the purposes of this paper, a condensed and simplified description of the PRAXIS diagnostic implementation is given; more complete details are covered in other work²³. The diagnostic uses a CO_2 , $10.6 \mu\text{m}$ -wavelength laser of about 40 W power as the source of incident electromagnetic radiation. As shown in Fig. 2(a), the initial beam is divided using a beam-splitter into two components: a primary beam and a local oscillator reference beam. The latter is frequency-shifted with respect to the initial laser frequency by 60 MHz using an acousto-optical deflector (AOD). Both beams are directed towards the plasma using a periscope and are focused to a beam waist of 3.58 mm inside the plasma with a lens. Their positions relative to one another arriving at the lens (separation and orientation) are fixed by bench optics such as a translator-rotator element. The intersection of the beams defines the observation volume, which, due to the milliradian angles of the beam intersection, extends over several centimeters. The optical setup incorporates infrared-compatible optics: ZnSe lenses and windows, highly-reflective gold-coated mirrors, and a liquid nitrogen-cooled HgCdTe detector to recover the scattered signal.

This diagnostic implementation uses a heterodyne detection scheme, in which the frequency-shifted local oscillator interacts with the scattered field from the plasma density fluctuations to produce an interference wave signal. The frequency shift of the local oscillator permits detection of spectra not around the initial laser frequency (in the THz range), but at a lower frequency (in the MHz range). The primary beam ($\sim 99\%$ of the initial laser power), in addition to contributing to the definition of the observation wave vector properties and the definition of an observation volume, provides a large-amplitude incident electromagnetic wave field for scattering on the density fluctuations. The primary beam is sent to an absorber after traversal of the plasma, as shown in Fig. 2(a).

The mixed local oscillator signal is transmitted to the detector. The detector signal, a time-varying voltage, is amplified and passed to a divider to form two identical channels. A reference signal from the acousto-optical deflector (at the modulation frequency of 60 MHz) is transmitted to a quadrature divider, such that two channels (now orthogonal in phase, forming *cos* and *sin* channels) are created. The *cos* and *sin* channels are now mixed with the detector channels, with a final filtering and amplification stage applied to each channel. This procedure is the signal demodulation stage and permits the recovery of the components of the complex scattered signal. The *cos* and *sin* components are recorded using a 14-bit acquisition card at high frequency (100 MHz) and sample depth (6.5×10^6 samples per channel). In these experiments, the thruster discharge current was simultaneously recorded on a 12-bit digital oscilloscope, triggered at the same time as the acquisition card.

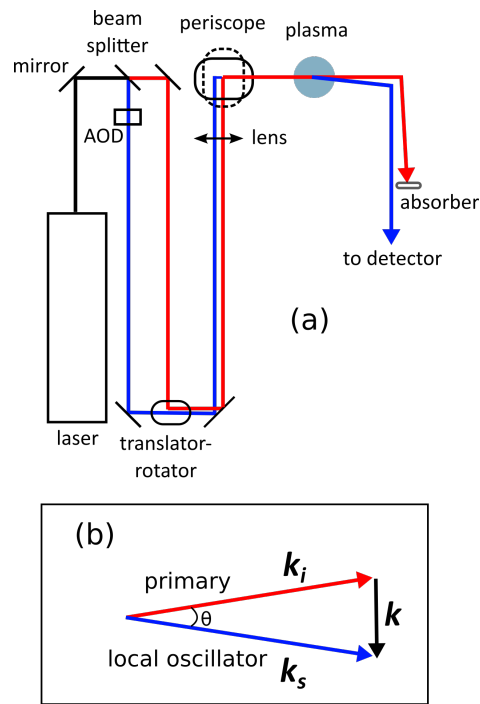


FIG. 2: Coherent Thomson scattering setup. (a) Simplified diagnostic optical configuration, showing the local oscillator (in blue) and primary beams (in red) for measurement within the plasma. The beams are focused in the plasma and after their subsequent divergence, the local oscillator, mixed with the scattered wave field, is transmitted to the detector. The primary beam is absorbed after traversal of the plasma. (b) Definition of the observation wave vector \mathbf{k} from incident (\mathbf{k}_i) and scattered (\mathbf{k}_s) wave vectors. The angle between the incident beams is θ .

Figure 2(b) shows the definition of the observation wave vector \mathbf{k} as the vector sum of the scattering wave vector \mathbf{k}_s and the incident wave vector \mathbf{k}_i , such that $\mathbf{k} = \mathbf{k}_s - \mathbf{k}_i$. The angle between the local oscillator and primary beams, θ , defines the magnitude of \mathbf{k} , as $|\mathbf{k}| = 2\pi/\lambda_i$, where λ_i is the wavelength of the incident laser. The maximum range of length scales which can be investigated ranges from 0.4 - 2 mm in this setup.

Figure 3 shows a view of the observation volume (formed by the overlap of the primary and local oscillator beams, in gray) and the cathode exit plane (in blue), to scale, and the x, y, z coordinate system defined in Fig. 1. The angular orientation of the observation wave vector \mathbf{k} in the xOz plane is defined using the angle α . An angle α of 0° is aligned with the cathode centerline, i.e., in the $+Oz$ direction. Negative angles in the range $[-180^\circ, 0^\circ]$ correspond to \mathbf{k} rotated from $+Oz$ clockwise to $-Oz$. The red and blue arrows depict the directions of, respectively, the primary and local oscillator beams. As α is varied, the angle of the observation wave vector with respect to the cathode centerline Oz (and with respect to the magnetic field) is changed.

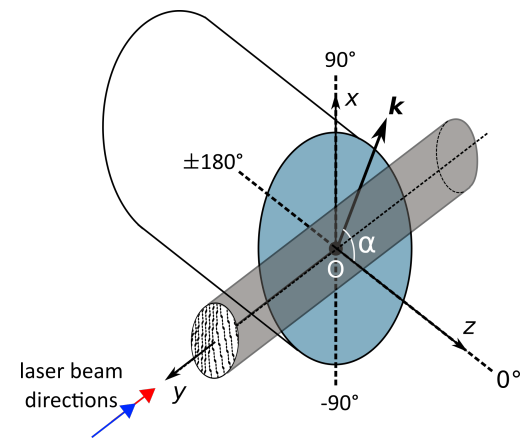


FIG. 3: View of observation volume (gray) relative to the cathode exit (blue). The x, y, z coordinate system of the observation volume is shown. The angle α defines the observation wave vector \mathbf{k} rotation angle in the xOz plane. Red and blue arrows depict the direction of the laser beams (primary, local oscillator) used to constitute the observation volume. The observation volume and cathode exit plane dimensions are shown to scale.

C. Spectral analysis and significance

The study of the signals which unambiguously originate from wave fluctuations requires acquisitions made under different conditions. These are made with (i) plasma and local oscillator present, (ii) plasma, local oscillator, and primary beams present, (iii) local oscillator and primary beams present, plasma absent and (iv) detector closed. These records, scaled to take into account variations of the DC detector current between the records, are used to calculate a normalized spectrum from which photonic noise (arising from the laser beams) and electronic noise (arising from thermal and amplifier noise) contributions have been removed.

To significantly reduce the signal variance, fast Fourier transforms are performed on segments of the signal, rather than the full length, and these Fourier transform spectra are then averaged. In this work, the segments used are of length 1×10^5 points, giving a frequency resolution of 10 kHz for the spectra.

The normalized spectrum, which we denote as $\Phi(\mathbf{k}, \omega)$, is multiplied by a scaling factor reflecting the characteristics of the scattering setup, to yield the dynamic form factor $S(\mathbf{k}, \omega)$, in units of seconds. This dynamic form factor is, in absolute units, a measure of the intensity of the density fluctuations over a frequency range, measured at the wavenumber value set for the experiment.

The relationship between the dynamic form factor and normalized spectrum⁵⁰ is written as

$$S(\mathbf{k}, \omega) = \frac{h\nu\pi\omega^2}{\eta P n_e L \lambda_i^2 \rho^2} \Phi(\mathbf{k}, \omega), \quad (1)$$

where h is Planck's constant, ν is the incident wave frequency, η is the detector efficiency, P is the laser power in

the scattering region, λ_i is the laser wavelength, ρ is the electron radius, w is the beam waist, and L is the plasma length traversed by the laser. In these experiments, $v = 2.83 \times 10^{13}$ Hz, $\eta = 0.62$, $P = 35.2$ W, and L is estimated to be 20 mm. Equation (1) assumes a local electron density n_e , which in these experiments is taken to be 10^{17} m^{-3} based on typical values of electron density measured for this cathode.

The mean square density fluctuation $\langle \tilde{n}^2 \rangle$ is derived from the dynamic form factor using the relation⁴⁶:

$$\langle \tilde{n}^2 \rangle = \frac{1}{(2\pi)^4} \int S(\mathbf{k}, \omega) d^3k d\omega, \quad (2)$$

which involves an integration over the full wavenumber and frequency space over which the fluctuations are present.

The use of the frequency-integrated *static* form factor $S(\mathbf{k})$ permits the comparison of the fluctuation intensities using a single absolute value, given by,

$$S(\mathbf{k}) = \frac{1}{2\pi} \int_{-\infty}^{\infty} S(\mathbf{k}, \omega) d\omega. \quad (3)$$

Discussions of the signal amplitudes measured will be made based on the static and dynamic form factors. The magnitude of the form factor provides a characterization of the turbulence intensity at the measurement length scales, in that values of $S(\mathbf{k}) \sim 1$ are associated with thermal plasmas, while $S(\mathbf{k}) \gg 1$ is associated with developed turbulence³². In subsequent discussions, the error in the calculation of the static form factor values is on the order of 10^2 .

III. MEASUREMENTS

In the following, the operating point is fixed for the thruster and cathode. The thruster is operated at 200 V and 0.6 mg/s xenon flow rate. The cathode is operated with a continuous heating current and voltage of 18 A and 11.5 V, respectively, and with a xenon flow rate of 1.2 mg/s. The chamber pressure during their simultaneous operation is 1×10^{-4} mbar.

The investigations of this work focus on: (i) the variation of the angular orientation of the observation wave vector, at a given wavenumber, in the xOz plane, and (ii) the variation of the wavenumber magnitude at a given angle in the xOz plane. In the angular investigations, the wavenumber magnitude is fixed at $k = 4740 \text{ rad/m}$ (corresponding to a length scale of 1.3 mm). In wavenumber variation experiments, measurements are performed at the fixed angle α of -80° , i.e., allowing for observation of fluctuations predominantly parallel to the magnetic field. All measurements are made at a fixed position d (see Fig. 1) of 10 mm.

A. Mode identification and classification

Variation of the angle α reveals the presence of distinct modes. To illustrate this, three angular positions from the investigations are selected and depicted in Fig. 4, seen in the xOz plane. The different directions of the observation wave

vector \mathbf{k} are shown by the red (Case *a*), blue (Case *b*) and black (Case *c*) arrows. The magnetic field map of the observation volume is also shown for comparison.

Figure 5 shows the dynamic form factor spectra obtained at each angle shown in Fig. 4. These plots use the same color for the spectra as for the corresponding wave vector orientations of Fig. 4. The three regions are characterized as follows.

- Case *a* ($\alpha = -65^\circ$, red), where \mathbf{k} is pointed 25° *outward* and away from the cathode, shows a low-amplitude, broad, negative frequency peak in the $\omega \in [-2, 0]$ MHz range, and symmetric peaks of frequency around ± 100 kHz. The MHz-frequency peak seen in all cases is in the expected frequency range for the ion acoustic mode originally identified in experiments^{15,51}. The mode dispersion relation presented later will support the classification of this mode as an ion acoustic mode.
- In Case *b* ($\alpha = -83^\circ$, blue), i.e., when \mathbf{k} is pointed nearly along the magnetic field lines, the symmetric peaks in the kHz range are not detected and the amplitude of the MHz-range peak increases. The magnetic field lines which traverse the observation volume point upwards towards the thruster (in the $+Ox$ direction). The observation of the negatively-signed MHz-frequency peak in Case *b* is compatible with fluctuations propagating in the direction antiparallel to the \mathbf{k} orientation but along the field lines.
- In Case *c* ($\alpha = -110^\circ$, black), i.e., when \mathbf{k} is pointed 20° *inward* and towards the cathode, a continued evolution in the peak amplitudes can be observed: the symmetric kHz-range peaks re-emerge, while the amplitude of the MHz-range peak decreases. In addition, a new low-amplitude, broad, positive-frequency peak in the MHz range simultaneously appears.

1. MHz oscillation

The presence of the broad, positive-frequency peak of Case *c* shows that the plasma wave has a component in the $-Oz$ direction, pointing toward the cathode orifice. Therefore, this observation indicates that a bi-directional plasma wave is formed in a certain range of angles with respect to the magnetic field lines. For an electrostatic current-carrying instability, when the *initial* electron Mach number $M_e = u_e/v_{th,e}$ (here u_e is the electron bulk velocity and $v_{th,e}$ is the electron thermal speed) is less than 1.3, it is known that the propagation of the plasma wave is only in the direction of the electron bulk velocity⁵². However, when $M_e > 1.3$, the amplitude of the plasma wave becomes large enough for a Buneman instability to be initiated⁵³.

The potential excitation of the Buneman instability in hollow cathodes, in the absence of a magnetic field, was first evoked by Mikellides *et al.* in Refs. 14 and 54. It was further proposed in Ref. 54 that runaway electrons may contribute to plasma turbulence. Hara and Treece⁵⁵ showed the transition from the current-carrying ion acoustic instability to the Buneman regime using 1D grid-based kinetic simulations. In Ref. 55, it was shown that the Buneman instability could generate, in addition to the expected ion

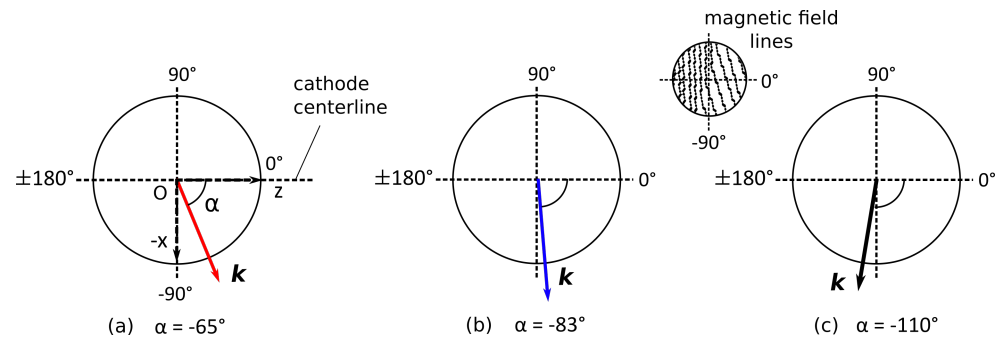


FIG. 4: Variation of the angle α of the observation wave vector \mathbf{k} relative to the cathode centerline. Three cases are shown: Case *a*: $\alpha = -65^\circ$ (red); Case *b*: $\alpha = -83^\circ$ (blue) and Case *c*: $\alpha = -110^\circ$ (black). Measurements at these angles permit observation of different mode types, seen in Fig. 5.

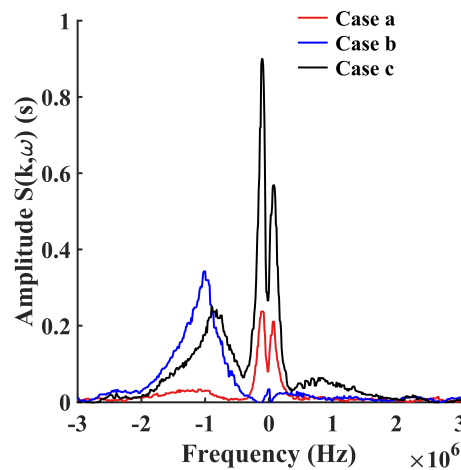


FIG. 5: Dynamic form factor spectra $S(\mathbf{k}, \omega)$ for varying orientations of the observation wave vector \mathbf{k} with respect to cathode centerline ($\alpha = 0^\circ$). Three cases are shown: Case *a*: $\alpha = -65^\circ$ (red); Case *b*: $\alpha = -83^\circ$ (blue) and Case *c*: $\alpha = -110^\circ$ (black), with a color scheme matching that of the angles depicted in Fig. 4.

acoustic waves propagating in the direction of the electron drift, backward-propagating fluctuations due to the large-amplitude plasma wave, which the linear perturbation theory of current-carrying plasmas does not account for. Such backward-propagating fluctuations could contribute to effects such as the formation of high-energy ions traveling toward the cathode orifice⁵¹. The theory and simulations suggest that the large-amplitude bi-directional plasma waves can be driven by an *initially* large electron Mach number, assuming plasma ions and electrons have Maxwellian energy distribution functions. However, the electron properties that one can measure in real systems are those of the *saturated* state. To understand the mechanisms of the instabilities and corresponding turbulence, comprehensive validation between experiments and simulations (in particular, multidimensional kinetic simulations) is required.

2. kHz oscillation

The observation of symmetric kHz-range peaks (around ± 100 kHz) shown in Cases *a* and *c*, together with their absence from Case *b* ($\alpha = -83^\circ$; blue), is intriguing.

In prior studies, different types of kHz-scale modes have been identified and characterized for cathodes operated with axial magnetic fields. Goebel *et al.*⁵¹ identified large-amplitude ionization oscillations (global and non-directive) in the 40 - 150 kHz range. Jorns and Hofer identified⁵⁶, for a thruster operating with a centrally-mounted cathode, an $m = 1$ azimuthally-rotating mode at the thruster centerline, also in the tens of kHz frequency range. Becatti *et al.*⁴¹ recently identified a kHz-frequency cathode oscillation categorized as a magnetohydrodynamic kink mode. The applied magnetic fields are in the Oz direction in these prior studies (parallel to the electric field), while the present configuration considers an externally-mounted cathode where the magnetic fields are in the Ox direction, i.e., perpendicular to the electric field along Oz .

In the present work, in order for the symmetric kHz peaks we have identified to be observed (as opposed to a single kHz peak of either sign), the observation volume must necessarily capture fluctuations which are both parallel and antiparallel to \mathbf{k} . The absence of the symmetric kHz peaks for Case *b*, where \mathbf{k} is oriented almost entirely along $-Ox$ and parallel to the magnetic field, means that observation of the kHz modes is restricted to wave activity in the yOz plane (and thus, predominantly perpendicular to the magnetic field lines). The plasma behaviors potentially consistent with the absence of symmetric kHz peaks in Case *b* include: (i) a traveling wave in the yOz plane, or (ii) standing waves generated by counter-propagating fluctuations along Oz ⁵⁷. We note, as an aside, that in this work, 20 kHz breathing mode oscillations have been measured in the discharge current. The spectral resolution shown in this work (10 kHz) prevents this breathing mode modulation from being discernible in the dynamic form factors (such as in Fig. 5).

Figure 6 illustrates plasma azimuthal drift (gray oval) in the yOz plane, where fluctuations in the directions indicated by the red arrows (parallel to Oz) would be perceived as peaks

of opposite signs for the observation volume aligned along Oy and with the observation wave vector \mathbf{k} possessing a component aligned with Oz . Generally, for the coherent Thomson scattering signal to be detectable, we must satisfy the following two conditions:

- a temporally-varying signal due to a traveling wave field, and
- spatial inhomogeneity at a particular length scale (or range of length scales) due to the density fluctuations produced by the wave.

A traveling wave field in the yOz plane can be excited by drift-driven instabilities. The $\mathbf{E} \times \mathbf{B}$ and diamagnetic drifts in yOz can potentially drive the emergence of coherent plasma structures or spokes, studied in various contexts and in recent computational work which incorporates the gradient of the magnetic field⁵⁸ and a Penning-type configuration where the applied magnetic field is homogeneous^{59–61}. It has been suggested that a similar type of drift instability (cf. lower hybrid drift instability) may play an important role in cross-field electron transport in Hall thruster and cathode plume plasmas⁶². The drift-driven instability theories predict positive wave growth rates over a wide range of wavenumbers, indicating that the partially-magnetized plasmas excite both small- and large-scale structures. The kHz-frequency modes detected at short length scales in this work may well reflect the presence of drift-driven fluctuations.

In the case of a standing wave plasma structure originating from the presence of counter-propagating waves⁵⁷, we would detect the individual counter-propagating waves as peaks of opposite signs, if \mathbf{k} is aligned parallel to their direction of motion. We cannot rule out this possibility as a potential explanation for the presence of the symmetric ± 100 kHz peaks. However, there is no evidence so far of any low-frequency, ionization-driven standing wave formation in the cathode plasma. This scenario would also likely be associated with a directivity for such fluctuations (the scattered signal would be maximized at the angle α for which \mathbf{k} points in the direction of wave motion). As will be seen later, there is no such strong directivity for the kHz-scale mode.

Further analyses (numerical and theoretical) would assist the classification of the detected kHz mode, given the configuration of fields in the observation volume and the local plasma parameters. Pending such analyses, we will identify these fluctuations as the “kHz-frequency drift-driven mode”.

The last illustrative case considered in Fig. 5 is Case *c* ($\alpha = -110^\circ$). At this angle, the symmetric peaks consistent with the kHz-frequency drift-driven mode reappear. In this case, the magnitude of the observation wave vector projection along the cathode centerline (perpendicular to the magnetic field) has increased only marginally with respect to Case *b*, but this is sufficient for the mode to become visible in the spectra. As the full angular exploration will show, there is a narrow range of angles for which the kHz mode is no longer observed, primarily for \mathbf{k} parallel to the magnetic field. The symmetry of the peaks in Fig. 5 for Case *c*, in frequency but not in amplitude, is potentially attributable to weak plasma density non-uniformities.

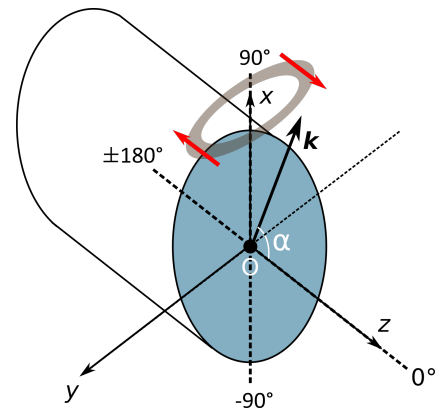


FIG. 6: Possible scenario for the observation of kHz frequency oscillations in the measurements. A plasma azimuthal drift (gray oval) in yOz is compatible with the experimental observation of peaks which are symmetric in frequency when the observation wave vector \mathbf{k} has a component pointing along Oz . Red arrows (parallel to Oz) depict the directions of the fluctuations which would be perceived by the measurement. As in Fig. 3, the observation volume (not shown) is along Oy .

B. Dependence of mode features on angle

More detailed information on the modes in Section III A can be obtained from a complete study of their angular characteristics. The dynamic form factor spectra, three examples of which are shown in Fig. 5, are determined for several angles (21 values) and the results are mapped in Fig. 7. The amplitudes plotted are the \log_{10} values of the dynamic form factor, $S(\mathbf{k}, \omega)$. This figure shows different characteristics of mode activity for both the kHz- and MHz-frequency modes as the angle α is varied, illustrated by the regions numbered 1 through 3. These regions will be discussed separately.

In Region 1, i.e., $\alpha \in [-170^\circ, -100^\circ]$, \mathbf{k} initially points primarily along the cathode centerline (in the direction $-Oz$) close to -170° , and near this angle, is aligned primarily perpendicular to the magnetic field lines. In this region, the kHz mode and MHz mode are both observed. Positive and negative frequencies for the MHz mode are visible, showing mode propagation in both the $+Oz$ and $-Oz$ directions. As the angle moves progressively towards -100° , \mathbf{k} is increasingly oriented away from the centerline and with an increasing vector component parallel to the magnetic field ($\alpha \rightarrow -90^\circ$). Here, the negative-frequency and positive-frequency MHz signals remain present, over an expanded frequency range. The presence of the positive-frequency MHz mode, coexisting with the negative-frequency MHz mode, indicates the presence of a bi-directional plasma wave, predicted by kinetic theory and 1D simulations⁵⁵, albeit under idealized conditions of a collisionless, homogeneous plasma with no applied magnetic field. As the plasma structure is complex, with inhomogeneous plasma density, current paths, and interaction with magnetic fields, it is possible that oblique electrostatic instabilities⁶³, such as the current-carrying ion-acoustic instabil-

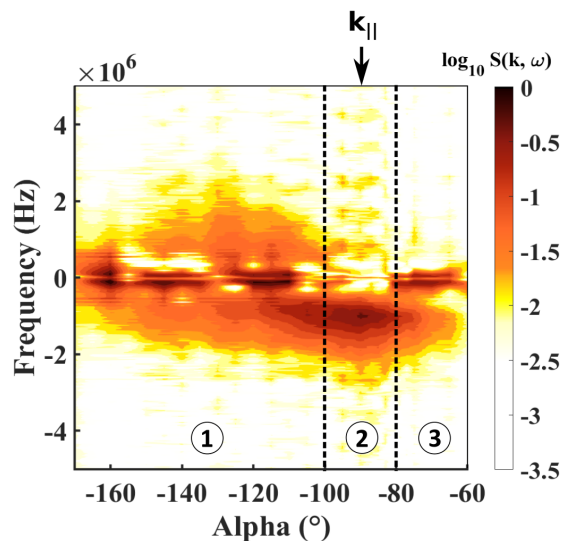


FIG. 7: Map of density fluctuation amplitudes (dynamic form factors, $\log_{10}S(\mathbf{k}, \omega)$) as a function of observation wave vector angle α , at fixed wavenumber $k = 4740$ rad/m.

The angular scan reveals the presence of kHz-scale symmetric oscillations and MHz-range oscillations, similar to Fig. 4. For the purposes of discussion, 3 regions are identified showing clear evolution in the characteristics and presence of the different modes. The angle corresponding to the direction along the magnetic field (-90°) is indicated by \mathbf{k}_{\parallel} .

ity and the Buneman instability, are present and their projected wave vector components are detected. As discussed in Section III A, numerical simulations (2D fluid⁵⁴ and 1D kinetic⁵⁵) suggest that the Buneman instability can be excited, with implications for particle transport and for the propagation direction of the ion acoustic modes. The bi-directional property of ion acoustic mode fluctuations which characterizes Region 1 suggests that such a transition from a mono-directional plasma wave to a bi-directional plasma may have occurred. We note that the MHz-frequency bi-directional modes are observed in Region 1 coexisting with the kHz-scale mode.

In Region 2, i.e., $\alpha \in [-100^\circ, -80^\circ]$, \mathbf{k} is predominantly parallel to the magnetic field. Here, with \mathbf{k} now oriented parallel to the magnetic field and perpendicular to the centerline, the kHz-scale modes are no longer observed. Simultaneously, the negative-frequency MHz mode reaches its peak amplitude but the positive-frequency MHz mode amplitude decreases, indicating that the plasma wave propagates in one direction towards the thruster along $+Ox$, along the magnetic field (see Fig. 2). Based on the comparison of the features seen in Region 1 and 2, it could well be the case that, while alignment of the electrons with the magnetic field does create conditions favoring electron acceleration and a transition to the Buneman regime, the resulting bi-directional perturbations are spread over angles not necessarily aligned with the magnetic field (and hence, are detectable in Region 1).

This could be a nonlinear effect best understood in a full 3D kinetic simulation. It should be noted that the periodic signal oscillations observable in Region 2, extending across the entire frequency range, are residual noise contributions.

Lastly, in Region 3, i.e., $\alpha > -80^\circ$, as the orientation of \mathbf{k} shifts further towards the $+Oz$ direction perpendicular to the magnetic field, a decrease in the negative frequency IAT-like mode amplitude is observed, along with a re-emergence of the kHz-frequency mode.

To conclude this section, we mention that a consideration of rotating plasma drift was not made in analyzing the MHz-frequency mode for the following reason. Judging from Fig. 7, the dominant direction for the MHz-mode propagation is parallel to the magnetic field (Region 2). There is no plasma rotation expected in the xOz plane. If we assume that the features observed in Region 1 are an extension of (or are driven by similar mechanisms to) those governing the observations in Region 2, the observation of oppositely-signed MHz frequency peaks could only correspond to the propagation of two distinct and separate perturbations, with wave vector components pointing along $+Ox$ and along $-Ox$. This bi-directional propagation appears to be a property of the MHz-frequency mode.

In the following sections, the observed modes will be examined further.

1. Comparison of fluctuations parallel and perpendicular to the magnetic field

The predominant orientation of the IAT-like, MHz fluctuations, in the direction parallel to the magnetic field as seen in Region 2 (see Fig. 7), points to the importance of the thruster magnetic field in creating directive motion of fluctuations produced at the cathode. The difference between MHz fluctuations in the directions perpendicular (\mathbf{k}_{\perp}) and parallel to the magnetic field lines (\mathbf{k}_{\parallel}) can be illustrated by a comparative plot of the dynamic form factors at two angles. This is shown in Fig. 8.

In Fig. 8, the red line shows the dynamic form factor spectrum for \mathbf{k} oriented at an α of -90° (\mathbf{k}_{\parallel}). MHz-frequency fluctuations are observable at a high amplitude and at negative frequency, which corresponds to the wave traveling in the $+Ox$ direction (see Fig. 3). In contrast, the spectrum measured at an angle such that \mathbf{k} is oriented near-perpendicular to the magnetic field at $\alpha = -170^\circ$ (\mathbf{k}_{\perp}), in blue, shows only comparatively low-level fluctuations. This figure further illustrates the directivity of the MHz fluctuations and their relationship to the magnetic field direction.

2. Mono- and bi-directional ion acoustic fluctuations

The observation of the MHz fluctuations primarily in the $+Ox$ direction (along the magnetic field and toward the thruster body) is likely because the electrons stream toward the thruster, where the higher potential exists. However, as noted earlier for Fig. 7, Region 1 ($\alpha \in [-170^\circ, -100^\circ]$) shows

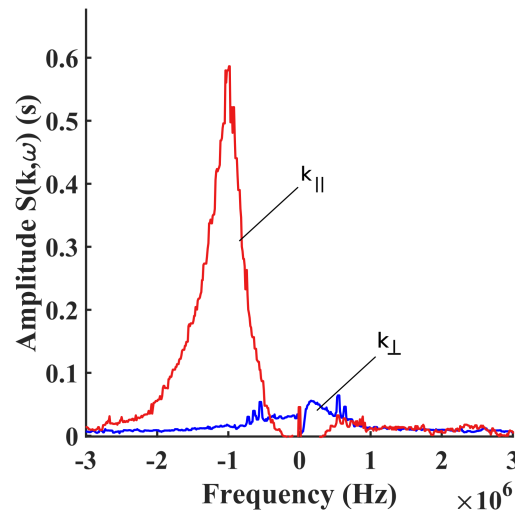


FIG. 8: Comparison of dynamic form factors observed in the directions parallel to the magnetic field (in red, $\alpha = -90^\circ$, $\mathbf{k}_{||}$) and near-perpendicular to the magnetic field (blue, $\alpha = -170^\circ$, \mathbf{k}_{\perp}).

evidence of a bi-directional plasma wave. The angular dependence of the IAT-like mode frequency and amplitude can be examined.

Figure 9 shows the variation of the negative peak frequency (black circles) and the positive peak frequency (red squares), obtained from the dynamic form factor spectra, over the angular range studied. The full error bar lengths in the frequency represent, here and throughout the paper, twice the Gaussian standard deviation. This is derived from a fit to the dynamic form factor profile where the mode is present (over the range $[0.3, 3]$ MHz and $[-0.3, -3]$ MHz). As previously mentioned, the low-level periodic signal extending over the $[-5, 5]$ MHz range in Region 3 is due to residual instrument noise. The vertical dashed line in the figure indicates the angle parallel to the magnetic field (-90°).

In Fig. 9, the mode frequencies depend on the angle α only to a small degree. This indicates that the phase velocity of the plasma waves detected at various angles have the same value, as the magnitude of the \mathbf{k} is fixed, i.e., here $k = 4740$ rad/m. The constant frequency observed across a wide range of α values confirms that the plasma wave is indeed ion acoustic-like, as the wave phase and group velocities are close to the ion acoustic speed, assuming that the ion bulk velocity is negligible. In Fig. 9 the error bar lengths are expected to be influenced by the diagnostic transverse resolution, which is written as $\delta k_t = \frac{\sqrt{2}}{w}$. From the beam waist of 3.58 mm, δk_t is 2482 rad/m. The angular investigations in this discussion, performed at a wavenumber of 4740 rad/m, give a ratio $\delta k_t/k$ of 0.5. This is consistent with a frequency width, for IAT peaks around a mean frequency of 1 MHz, of 500 kHz. This width is close to the error bar lengths shown on Fig. 9. The shapes of the signal profiles are more peaked than standard Gaussians and exhibit tails

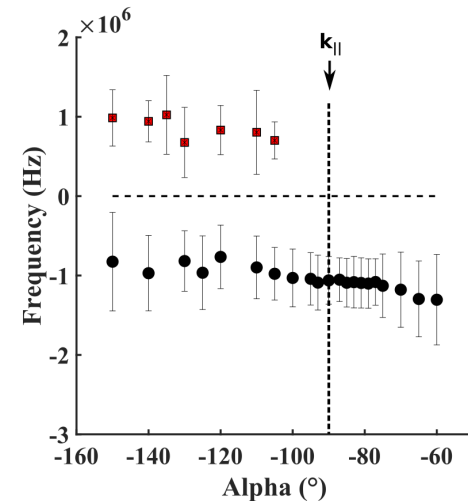


FIG. 9: Frequency variation of the ion acoustic-like mode as a function of \mathbf{k} orientation angle α , showing negative frequencies (black circles) and positive frequencies (red squares). Error bar length is twice the Gaussian standard deviation. The vertical dashed line indicates the orientation angle parallel to the magnetic field (-90°).

extending towards higher frequencies (seen for example, in Fig. 8); in other studies, for example in Ref. 46, some deviation from expected spectral shapes is attributed to nonlinear effects, however, understanding such contributions would require dedicated modeling.

Figure 10 shows, at each angle, the integrated amplitude or static form factor (Eq. 3) determined over the frequency range in which MHz fluctuations are present ($[0.3, 3]$ MHz and $[-0.3, -3]$ MHz). Both negative (black circles) and positive frequency peak (red squares) points are shown. The vertical dashed line in the figure indicates the angle parallel to the magnetic field (-90°). One interesting feature is the difference in the angular range over which the negative and positive frequency peaks are observed, and their corresponding amplitudes. The negative-frequency peak dominates in amplitude, and a Gaussian fit line (black full line) is made to this data. As noted before, the dominance of these fluctuations can be primarily attributed to electron extraction and transport toward higher potential, i.e., the thruster, in the $+Ox$ direction. On the left-wing angles of the negative-frequency peaks (black symbols) in the range $\alpha \in [-150^\circ, -125^\circ]$, there is clear deviation from the Gaussian profile of the fitted points: the amplitudes on the $\alpha \in [-150^\circ, -125^\circ]$ wing decrease far more gradually than would be expected. This indicates that the electrostatic instability is not only in the direction purely parallel to the magnetic field, but has some oblique components. In particular, the electron path from the hollow cathode to the thruster may occur in a wide angle, which depends on the cathode coupling voltage and facility effects⁶⁴. Fluctuations in the \mathbf{k}_{\perp} direction appear to have a fundamentally different character from those observed predominantly around

This is the author's peer reviewed, accepted manuscript. However, the online version of record will be different from this version once it has been copyedited and typeset.

PLEASE CITE THIS ARTICLE AS DOI: 10.1063/5.0071650

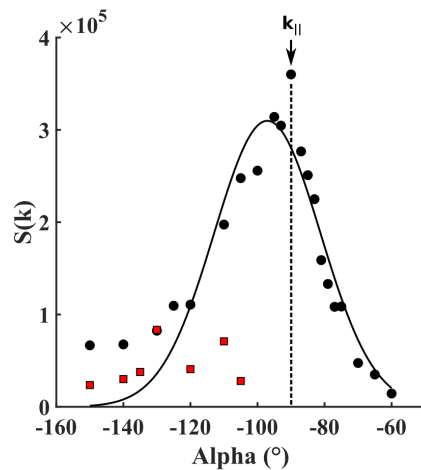


FIG. 10: $S(\mathbf{k})$ variation for the ion acoustic mode as a function of orientation angle α (negative frequency peak - black circles; positive frequency peak - red squares). The angular exploration is performed at a fixed wavenumber of 4740 rad/m. A Gaussian profile fit is applied to the amplitude variation over the full range of angles for the negative frequency peak (black line). The vertical dashed line indicates the orientation angle parallel to the magnetic field (-90°).

the \mathbf{k}_{\parallel} direction. A dedicated angular exploration focusing primarily on the \mathbf{k}_{\perp} direction (centered around the angle -180°) could help clarify these differences.

For the negative-frequency MHz peak, the values determined from a fit to the points in Fig. 10 are the source of additional information on the mode. From the fit (black line), optimized parameters of the amplitude, the Gaussian center angle μ_0 , and angular width σ_0 are obtained as 3.1×10^5 , -97° and 15.9° , respectively. The center angle value is only 7° away from the \mathbf{k}_{\parallel} propagation direction of -90° . As discussed with reference to Fig. 1, there is a 16° angular opening in the field line direction within the observation volume and thus finding fluctuations centered around a center angle of -97° still suggests propagation parallel to the magnetic field. It is also worth noting that the diagnostic angular resolution, for the given laser waist and the fixed observation wavenumber used during this investigation of 4740 rad/m, is 4.77° . Taking these effects into account, it is reasonable to conclude that the main direction of propagation we calculate from the data of Fig. 10 is indeed along the \mathbf{k}_{\parallel} direction. A further observation of some significance is the fact the angular opening of the magnetic field lines in the observation volume, 16° , is very close to the standard deviation of the Gaussian fit σ_0 determined for the mode (15.9° , when corrected for the device resolution, 15.1°). This suggests not only propagation of the wave parallel to the magnetic field, but also its restricted angular extent, the breadth of which is dictated by the variations of the magnetic field line inclination within the observation volume.

On the other hand, the positive-frequency peak data, in red

in Fig. 10, show weaker but unambiguous fluctuations approaching angles pointing not towards the thruster, but towards the cathode orifice. While the ions in the hollow cathode plume plasma will be attracted to the lower potential, i.e., inside the hollow cathode, the detection of positive-frequency MHz modes likely indicates the formation of a bi-directional plasma wave induced by a large amplitude kinetic instability⁵⁵, as discussed earlier in the paper. The IAT fluctuations reach significant amplitudes, as illustrated by Fig. 10, corresponding to density fluctuation levels which are orders of magnitude larger than the thermal levels. Quantifying these fluctuation levels in terms of a potential amplitude requires the use of simplifying assumptions which we will not make in this work. Linear kinetic theory fails at the description of such large-amplitude waves^{52,55}. However, the unambiguous detection of saturated fluctuations with components aligned anti-parallel to the magnetic field provides evidence that bi-directional waves are excited. Fluctuations of these types of ion acoustic waves, propagating towards the cathode, may play a role in cathode erosion, for example⁵¹. The variation in amplitudes of these positive-frequency peaks does not show a clear trend. Unlike the dominant negative-frequency MHz mode, which points mainly parallel to the magnetic field and towards the thruster, the positive-frequency mode is observed in an angular range which indicates propagation with a significant \mathbf{k}_{\perp} component.

3. kHz-frequency drift-driven mode

The observation of the kHz-frequency drift-driven mode in the yOz plane for most angles, except for the angles where \mathbf{k} is parallel to the magnetic field, is already evident from Fig. 7. The variation in frequency of this mode with angle is shown in Fig. 11. A Gaussian fit to both negative and positive dynamic form factor peaks is used to determine the central frequencies (red squares for positive and black circles for negative frequencies) and the Gaussian standard deviation. Figure 7 shows a gap in the plotted points in the angular range $\alpha \in [-110^\circ, -81^\circ]$ in which the kHz-frequency peaks are absent (for example, illustrated by Case *b* in Fig. 5 at -83° and Region 3 in Fig. 7). This region corresponds, as discussed earlier, to \mathbf{k} oriented near-parallel to the magnetic field lines; the kHz-frequency fluctuations appear to propagate perpendicular to the magnetic field, in the yOz plane.

As seen in Fig. 12, the kHz-frequency mode amplitude does not show a clear dependence on angle. The form factor amplitudes of the positive (red squares) and negative (black circles) peaks corresponding to the points in Fig. 11 are shown. The form factor values indicate significant density fluctuation levels, on the same order as, but approximately half of, those determined for the MHz-frequency modes.

C. Dependence of mode features on length scale

A map of the dynamic form factors at different wavenumbers, shown in Fig. 13, illustrates clearly how the fluctua-

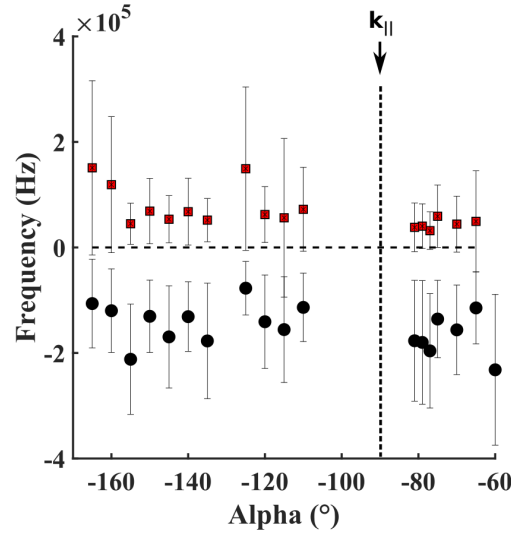


FIG. 11: Frequency variation of the kHz-frequency drift-driven mode as a function of \mathbf{k} orientation angle α (red squares: positive frequencies, black circles: negative frequencies). The vertical dashed line indicates the orientation angle parallel to the magnetic field (-90°). Error bar length is twice the Gaussian standard deviation.

tion intensities of the modes vary over different length scales. Measurements are made at a fixed angle $\alpha = -80^\circ$ i.e., close to the \mathbf{k}_{\parallel} direction. At this angle, the ion acoustic-like mode is near the angle at which it attains its maximum amplitude. It should be noted that while the kHz-frequency fluctuations are discernible at this angle of $\alpha = -80^\circ$, as seen in Fig. 7, they are absent in the purely parallel direction where $\alpha = -90^\circ$ (as shown by Fig. 7).

In Fig. 13, both the kHz and ion acoustic modes are visible. The kHz mode is evident at all wavenumbers as a band of symmetric signals centered around 0 MHz. The ion acoustic mode, on the other hand, shows a clear frequency dispersion, evolving to higher (negative) frequencies as the wavenumber increases and simultaneously decreasing in amplitude. At the angle chosen for this investigation ($\alpha = -80^\circ$), as seen in Fig. 7, positive frequency fluctuations of this mode were absent. We shall focus on the dispersion characteristics of the dominant negative frequency mode, propagating along the magnetic field lines towards the thruster.

1. Mono-directional ion acoustic (MHz) fluctuations

The ion acoustic-like mode has a linear dispersion relation as seen in Fig. 14. The group velocity v_g determined from the slope of the plotted points is 1.3 ± 0.17 km/s. From the kinetic dispersion relation of the electrostatic, unmagnetized, current-carrying, ion-acoustic instability^{52,55}, assuming that the ion drift velocity is negligible, the real frequency ω_r and

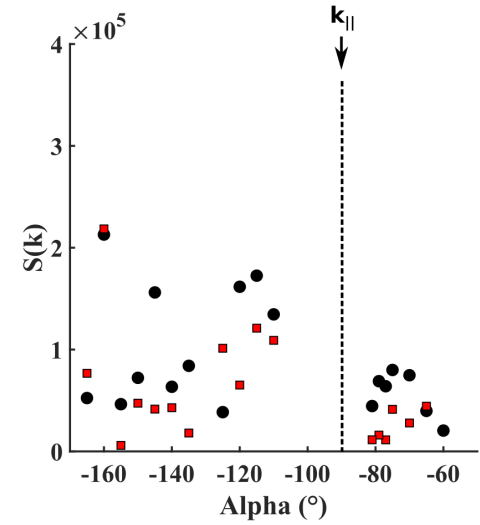


FIG. 12: $S(\mathbf{k})$ variation of the kHz-frequency drift-driven mode as a function of \mathbf{k} orientation angle α (red squares: positive-frequency peaks, black circles: negative-frequency peaks). The vertical dashed line indicates the orientation angle parallel to the magnetic field (-90°).

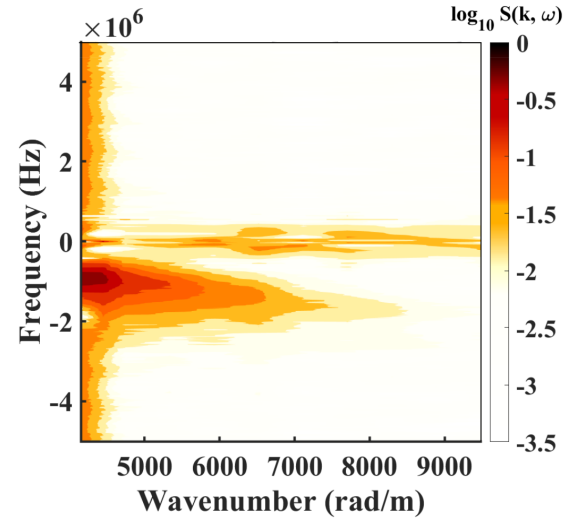


FIG. 13: Density fluctuation amplitudes (dynamic form factors, $\log_{10}S(\mathbf{k}, \omega)$) as a function of the magnitude of the wavenumber, at fixed angle ($\alpha = -80^\circ$). Both kHz-frequency and MHz-frequency modes are visible.

growth rate γ are given by

$$\omega_r = kc_s, \quad (4)$$

$$\frac{\gamma}{\omega_r} \approx \sqrt{\frac{\pi}{8}} \left[\sqrt{\frac{m_e}{m_i}} \left(\frac{u_d}{c_s} - 1 \right) - \left(\frac{T_e}{T_i} \right)^{3/2} \exp \left(-\frac{T_e}{2T_i} \right) \right], \quad (5)$$

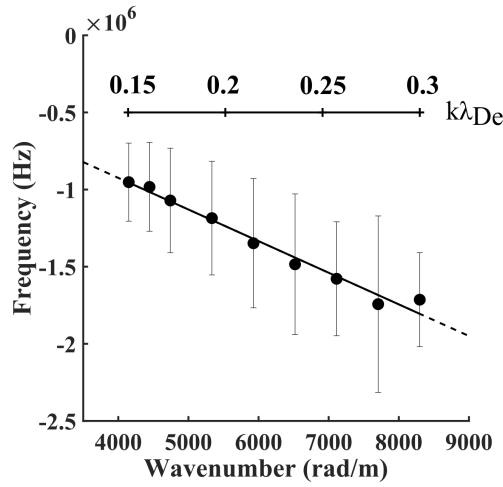


FIG. 14: Dispersion relation of the primary ion acoustic mode. The error bar length is twice the Gaussian standard deviation. The group velocity v_g determined from the slope of the plotted points is 1.3 ± 0.17 km/s. A $k\lambda_{De}$ axis is also shown, determined based on local plasma parameters.

where ω_r is the mode frequency in rad/s, $c_s = (k_B T_e / m_i)^{1/2}$ is the ion acoustic speed, k_B is the Boltzmann constant, $u_d = u_e - u_i$ is the streaming velocity between electrons and ions, u_i is the ion drift, m_e and m_i are electron and ion masses, respectively, and T_e and T_i are electron and ion temperatures, respectively. Equation (5) shows that the growth rate is positive when $u_d > c_s$ in the limit of $T_e \gg T_i$ (i.e., $u_e > c_s$ if $|u_e| \gg |u_i|$). The last term in Eq. (5) corresponds to ion Landau damping.

On equating the measured value of group velocity to the ion acoustic velocity c_s , we obtain a local electron temperature which is 2.3 eV. This value is consistent with typical electron temperatures of a few eV for such cathodes⁶⁵. The value of the y-intercept of Figure 14 is -104 kHz, determined from the unconstrained fit. This value is negligible in comparison with the error bar width, confirming the ion acoustic-like nature of the wave spectrum. The electron Debye length is determined assuming a local electron density of 10^{17} m^{-3} and the electron temperature of 2.3 eV determined from the experimental dispersion relation. This yields a value of $3.6 \times 10^{-5} \text{ m}$ for λ_{De} , which is used to plot $k\lambda_{De}$ in Fig. 14.

In the presence of an ion drift, the wave phase (and group) velocities are given by,

$$\frac{\omega_r}{k} = c_s + u_i. \quad (6)$$

In Ref. 15 and Ref. 18, the phase velocity measured using dual ion saturation probes exceeds the value of c_s due to the presence of a large on-axis ion drift velocity.

In our case, the configuration (electrons bending away from the axial cathode electric field due to the orthogonal magnetic field) involves a different potential structure which appears to justify the neglect of the ion velocity along the direction in which the dispersion relation is measured (near-

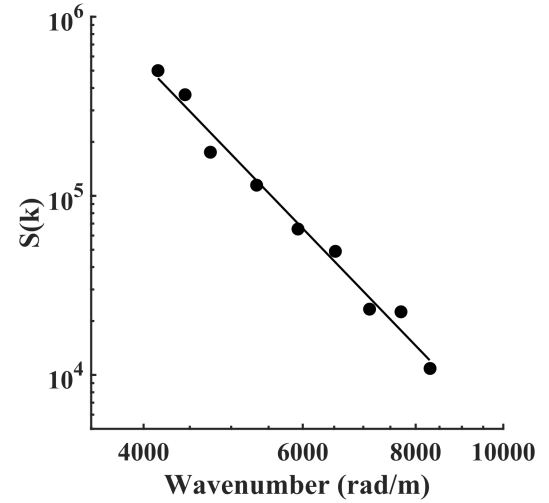


FIG. 15: Integrated density fluctuation amplitude $S(\mathbf{k})$ of the ion acoustic mode as a function of wavenumber on log-log scales. A linear fit to the points gives a $k^{-5.2 \pm 0.58}$ scaling.

parallel to the magnetic field lines). The comparatively low ion velocities in this direction may well account for the smaller group velocity observed in our measurement (equal to c_s), in comparison to other cases from the literature.

The variation of the fluctuation intensity with wavelength is of particular interest for characterizing turbulence. The form factor variation with wavenumber for the ion acoustic mode is shown in Fig. 15, plotted on log-log scales. A clear power law is identifiable over the range of wavenumbers explored, where $S(k) \propto k^m$. For the data of Fig. 15, m is -5.2 ± 0.58 . This value is interesting to consider in the context of scaling law investigations which have been previously performed for ion acoustic turbulence.

Kadomtsev determined analytically a k^{-3} scaling for the spectrum of the ion acoustic mode energy in the absence of a magnetic field, of the form $k^{-3} \ln(k\lambda_{De})^{-1}$. This relation was established by considering the energy balance of the system in the presence of a linearly growing mode and dissipation by ion-neutral collisions. The Kadomtsev scaling has been found in other works, including in studies of ion acoustic turbulence in collisionless shock experiments⁶⁶ using coherent Thomson scattering. In Ref. 66, in addition to recovering the scaling parameter value of -3 , the authors observed Kadomtsev's predicted cutoff at a $k\lambda_{De}$ value of ~ 1 . This cutoff is not identifiable within the range of wavenumber values used in the present experiments, as shown in Fig. 14.

The scaling of -5.2 ± 0.58 found in this work represents strong deviation from Kadomtsev's case. The Kadomtsev power law is not universal, and the assumptions on which it is based (a Maxwellian electron energy distribution function, neglect of linear Landau damping on ions for $T_i \ll T_e$, unmagnetized plasma) are not necessarily valid for our case, and indeed, for many other plasmas. An early analytical study by Nishikawa and Wu⁶⁷ demonstrated the non-universality of the Kadomtsev scaling. That work showed

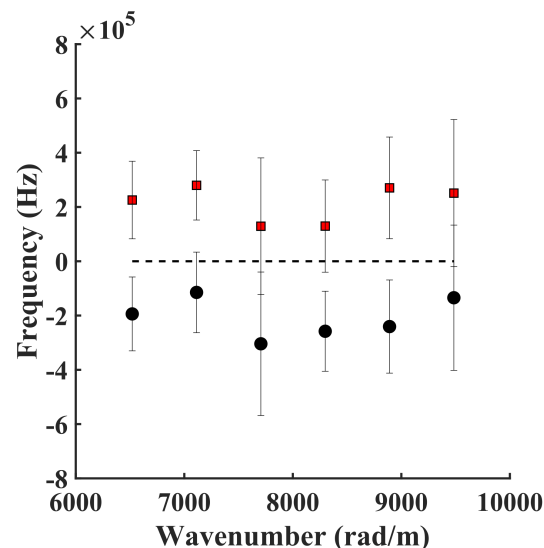


FIG. 16: Frequency of positive (red squares) and negative frequency (black circles) peaks measured for the rotating kHz-scale mode, as a function of wavenumber. Error bars have lengths of twice the Gaussian standard deviation.

that electron trapping could be a dominant effect modifying the saturated turbulent spectrum. In their case, an IAT scaling law of the form $k^{-13/3}$ was found. The importance of the balance between trapping and collisional effects in determining the energy scaling was supported by the experimental work of Yamada and Raether⁶⁸.

2. kHz-frequency drift-driven mode

The kHz-frequency mode does not exhibit a frequency dispersion. This can be seen in Fig. 16, where the frequencies of both negative and positive frequency peaks (i.e., the signals measured due to the propagation of the mode through the observation volume) show a mostly flat variation with wavenumber.

Figure 16 demonstrates the expected symmetry in frequency and similar trends for the positive (red squares) and negative (black circles) peaks. The error bars shown have lengths of twice the Gaussian peak widths. Mode frequencies are observed to be below 300 kHz. The observation volume length does not allow a localization of the fluctuations along y , nor does it permit us to say at present whether observation of these kHz fluctuations could be associated with any particular spoke-like rotating modes. Such information could potentially be gained from camera imaging, which has been applied to study coherent structures in the cathode plasma previously, such as in Ref. 56. Indeed, in a very recent study, Hepner *et al.*⁶⁹ demonstrated via fast camera imaging the presence of a rotating coherent structure ($m = 1$ mode) in the plasma of an externally-mounted cathode operated with a thruster, which resembles our own configuration.

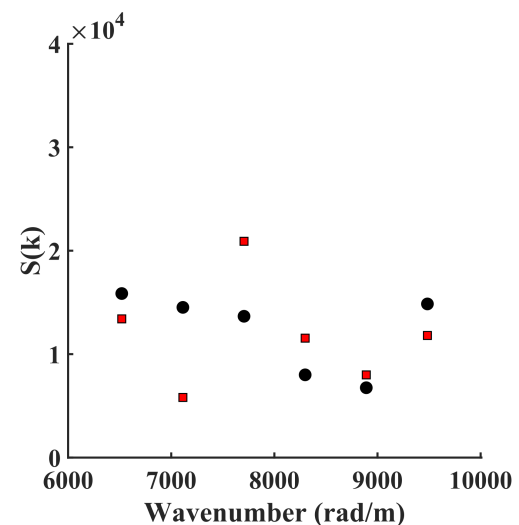


FIG. 17: Form factor of positive (red squares) and negative frequency (black circles) peaks measured for the rotating kHz-scale mode, as a function of wavenumber.

The variation in fluctuation amplitude with the wavenumber is flat, as shown by Fig. 17. This figure shows the variation for positive (red squares) and negative (black circles) frequency peaks. The static form factor magnitude is independent of measurement length scale and similar for both frequency peaks, which could be expected from the frequency-wavenumber characteristics of Fig. 16.

IV. DISCUSSION

The wider significance of some of the observations made in this work may be considered, particularly in light of the existing literature.

The CTS implementation described in the current work is valuable in part due to the high degree of angular selectivity of the diagnostic, which allows precise information on the direction of wave propagation to be determined. The observation of wave propagation along the magnetic field, arising as one consequence of the electron magnetization, is perhaps unsurprising. However, the degree of angular collimation of ion acoustic mode (MHz) fluctuations in the presence and absence of a magnetic field is highly variable across the literature.

We may first consider the unmagnetized plasma case. Kadomtsev¹⁰ expected that ion acoustic waves would develop in a narrow cone in the case of propagation within a confined geometry, due to absorption of waves propagating perpendicular to the electron stream, while in an unbounded plasma, the propagation cone angle could extend to 90°. In experimental work on unmagnetized columns, the angular opening of fluctuations around the main electron drift direction was found to be as small as 3° (Ilić⁷⁰) and as large as 60° (Yamada and Raether⁶⁸ and Slusher⁷¹). It is worth not-

ing that Sleeper *et al.*⁷² performed an important analytical study of the 3D spectrum of ion acoustic mode fluctuations in an unmagnetized geometry which predicted a broad angular spread of fluctuations (tens of degrees) around the electron drift direction, with a strong dependence of the angular spread on the electron-ion temperature ratio. Many experimental results appear to confirm the expected angular spread of fluctuations of tens of degrees.

The situation in the case of plasma magnetization is even more complex. In our work, we have measured an angular width of the fluctuations (σ_0) of 15° , a value reflecting the degree of divergence of magnetic field lines in the observation volume. Hirose *et al.*⁷³ showed analytically that the extent of electron Landau damping varied with the mode propagation angle with respect to the magnetic field. This could provide one reason as to why there is such a marked difference in the amplitude of the parallel and perpendicular fluctuation levels observed in this work (Fig. 8).

In the present work, the dispersion relation for ion acoustic turbulence and the mode angular propagation have been studied at much shorter length scales than have been analyzed in previous work, such as in Ref. 15. The wavenumbers in the present study are in the range $k \in [2.5 \times 10^4, 5.7 \times 10^4] \text{ m}^{-1}$, compared to up to 3000 m^{-1} in Ref. 15. It is interesting to consider which length scales may be important for wave-particle interactions. In this study, our observations suggest nonlinear behavior at short length scales: the possible appearance of the Buneman instability as the cause of bi-directional IAT propagation, and deviations from the Kadomtsev unmagnetized power scaling law. It is possible, given the detection of the IAT fluctuations across a range of length scales, that its action on particles extends over a wide range of wavenumbers (and that interaction may vary according to whether particles are magnetized). The same complexity of interaction may govern modes such as the kHz-scale drift-driven mode observed in the present work. Ultimately, these experimental observations will need to be complemented with high-fidelity numerical simulations.

This work highlights the need for simulations which are (i) 3D, in order to capture complex spatial effects and mode propagation which appear to be driven by the electron magnetization and deviation from the cathode centerline, (ii) kinetic, in order to capture effects such as bi-directionality (not evident from fluid codes), which were seen in 1D simulations⁵⁵, and (iii) multiscale, i.e., permitting investigation of the nonlinear coupling between small-scale turbulence and large-scale coherent structures⁷⁴.

V. CONCLUSIONS

In this manuscript, the presence of unstable modes in both kHz and MHz frequency ranges in a hollow cathode operating in proximity to a Hall thruster and subject to magnetization has been investigated.

Distinct modes have been identified using coherent Thomson scattering. These are:

- a mono-directional ion acoustic wave in the MHz fre-

quency range, propagating in a direction predominantly parallel to the magnetic field, and with an angular width of 15° around the magnetic field direction,

- bi-directional ion acoustic mode fluctuations in the MHz range, potentially the consequence of the excitation of a large-amplitude plasma wave that could be driven by Buneman-type instabilities,
- electron density fluctuations in the kHz range which appear to be a consequence of plasma azimuthal drift in the plane perpendicular to the magnetic field.

To our knowledge, this is the first application of coherent Thomson to the measurement of multiscale oscillation modes in a hollow cathode applied to electric propulsion and coupled to a Hall thruster. This experimental implementation exploits the angular selectivity of the coherent Thomson scattering diagnostic in order to obtain detailed information regarding mode propagation and its link to the magnetic field. The mono-directional ion acoustic mode fluctuations exhibit a linear dispersion relation (group velocity $1.3 \pm 0.17 \text{ km/s}$). The mode shows a power scaling law ($k^{-5.2 \pm 0.58}$) which deviates from the Kadomtsev scaling for unmagnetized ion acoustic turbulence (k^{-3}) and is suggestive of nonlinear effects in mode saturation; such effects have yet to be clarified but may be elucidated in appropriate numerical simulations. These findings, overall, highlight the interest of laser scattering for detailed characterization of cathode modes and the possibility of accessing new information regarding energy, dispersion and the angular characteristics of unstable modes, particularly at millimetric and submillimetric length scales. Much remains to be understood in the configuration used in this work. These complex wave dynamics observed in the cathode plasma could play a role in particle heating and transport, and thus, in the nature of the cathode operating regimes and cathode-thruster coupling.

ACKNOWLEDGMENTS

ST thanks T. Lejosne and T. Dubois, and especially thanks the reviewers for their insightful comments. KH acknowledges the support by the US Department of Energy, Office of Science, Office of Fusion Energy Sciences, under Award No. DE-SC0020623 and the Air Force Office of Scientific Research under Awards No. FA9550-18-1-0090 and No. FA9550-21-1-0433.

DATA AVAILABILITY STATEMENT

The data that support the findings of this study are available from the corresponding author upon reasonable request.

¹D. M. Goebel, G. Becatti, I. G. Mikellides, and A. Lopez Ortega, "Plasma hollow cathodes," *Journal of Applied Physics* **130**, 050902 (2021).

²D. R. Lev, I. G. Mikellides, D. Pedrini, D. M. Goebel, B. A. Jorns, and M. S. McDonald, "Recent progress in research and development of hollow cathodes for electric propulsion," *Reviews of Modern Plasma Physics* **3**, 1–89 (2019).

³D. R. Lev, G. D. Emsellem, and A. K. Hallock, "The rise of the electric age for satellite propulsion," *New Space* **5**, 4–14 (2017).

This is the author's peer reviewed, accepted manuscript. However, the online version of record will be different from this version once it has been copyedited and typeset.

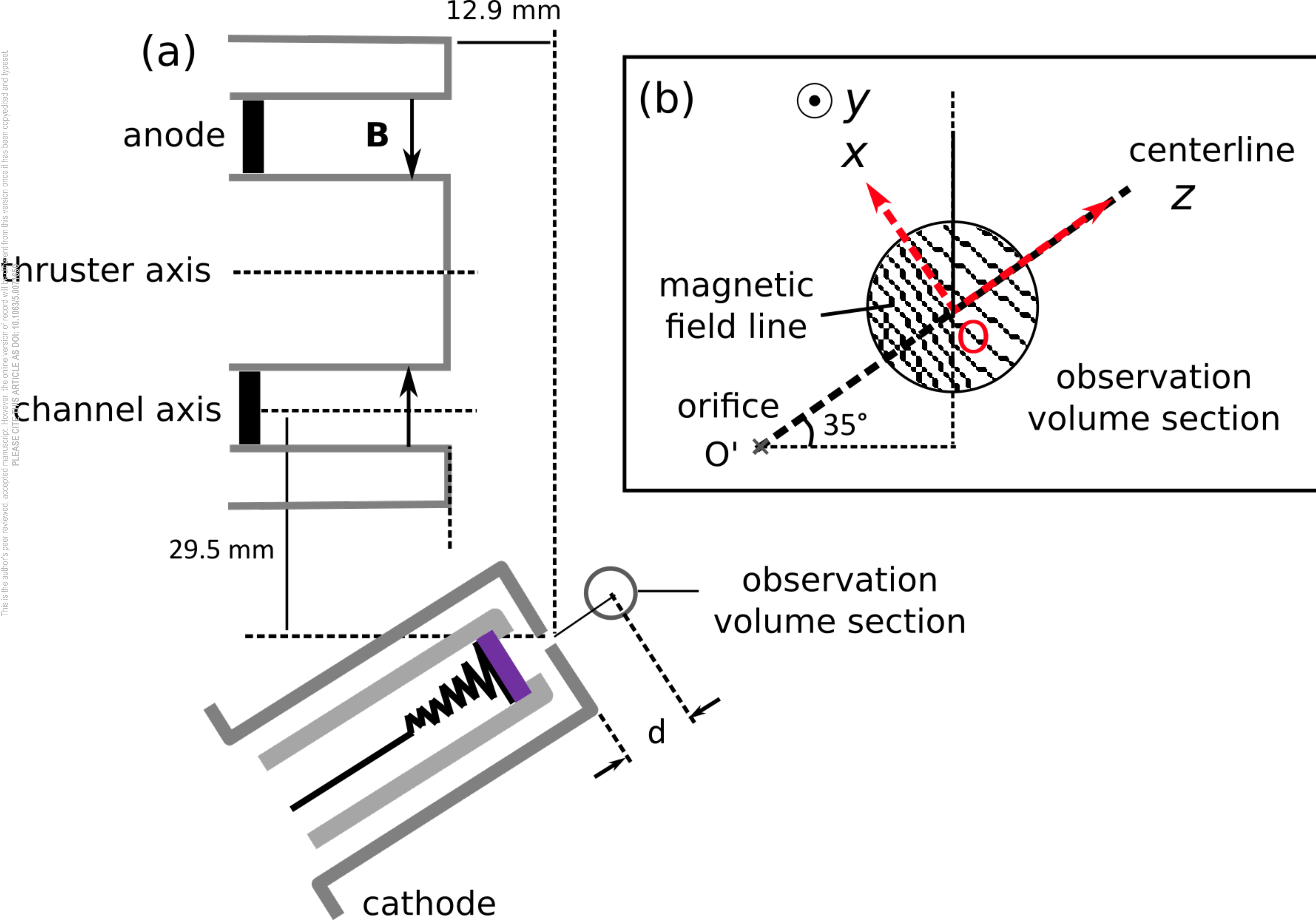
PLEASE CITE THIS ARTICLE AS DOI: 10.1063/5.0071650

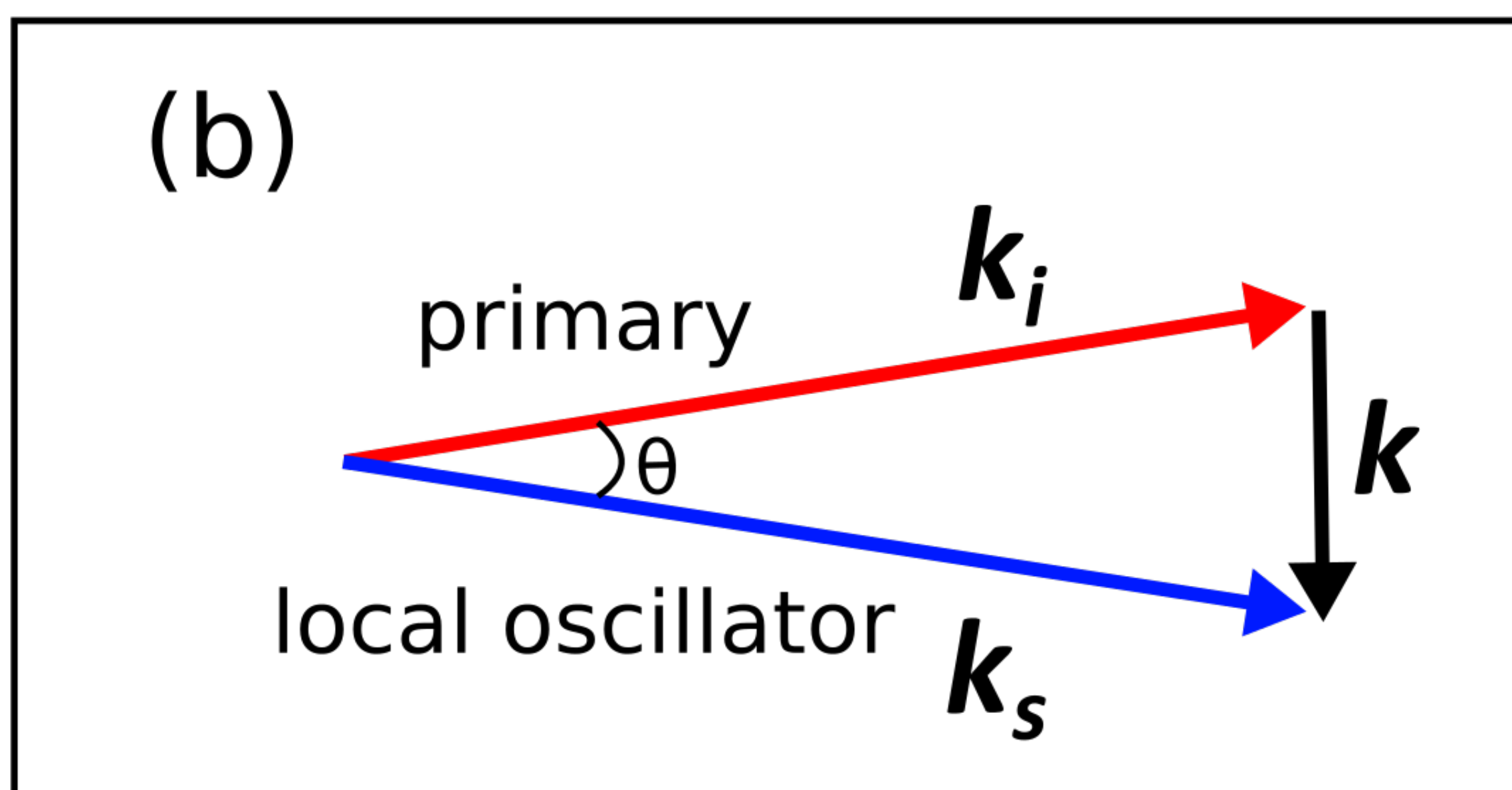
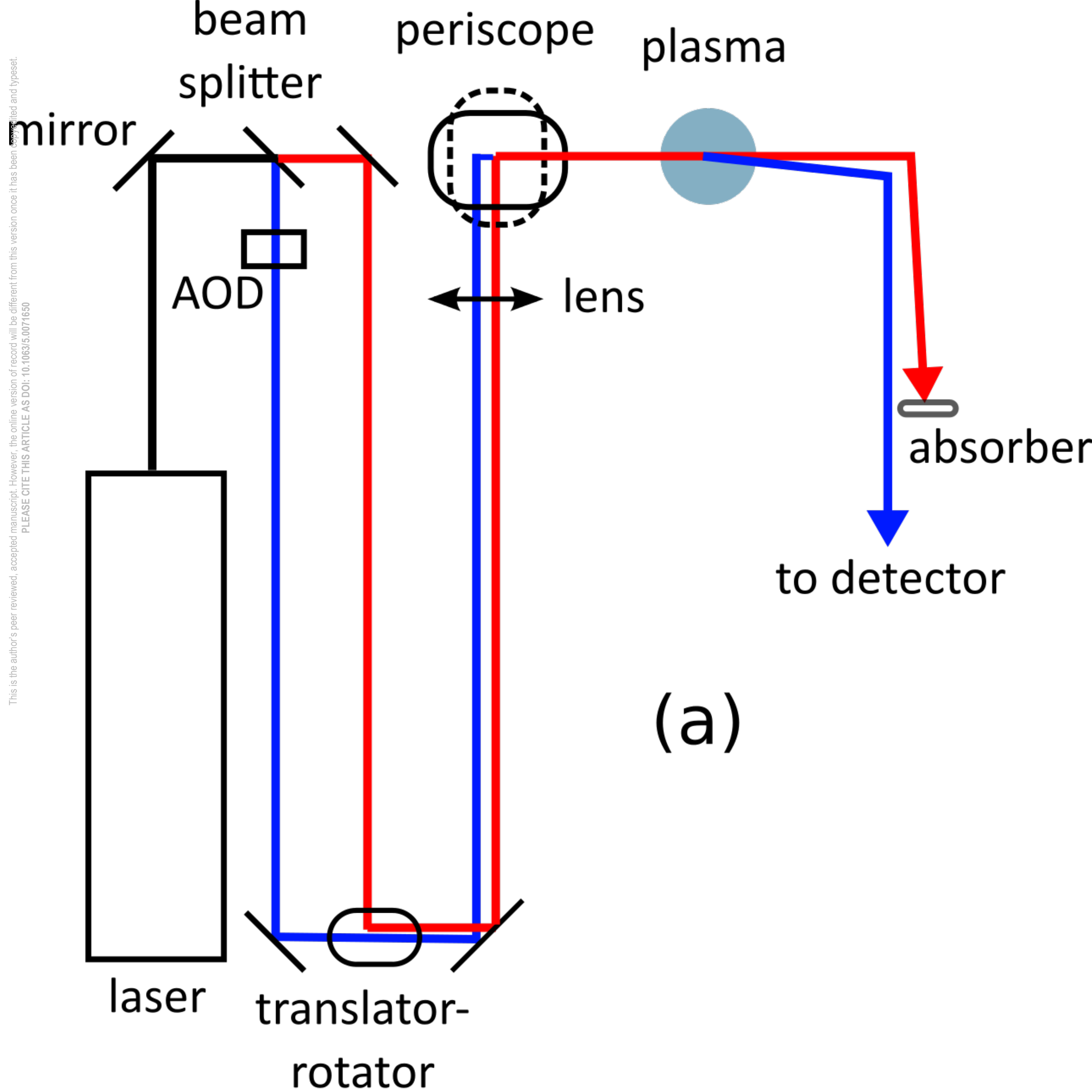
- ⁴K. Lemmer, "Propulsion for cubesats," *Acta Astronautica* **134**, 231–243 (2017).
- ⁵J. D. Sommerville and L. B. King, "Hall-effect thruster–cathode coupling, part i: Efficiency improvements from an extended outer pole," *Journal of Propulsion and Power* **27**, 744–753 (2011).
- ⁶J. D. Sommerville and L. B. King, "Hall-effect thruster–cathode coupling, Part II: Ion beam and near-field plume," *Journal of Propulsion and Power* **27**, 754–767 (2011).
- ⁷K. K. Jameson, D. M. Goebel, R. R. Hofer, and R. M. Watkins, "Cathode coupling in Hall thrusters," in *30th International Electric Propulsion Conference* (Citeseer, 2007) pp. 2007–278.
- ⁸E. R. Priest and J. J. Sanderson, "Ion acoustic instability in collisionless shocks," *Plasma Physics* **14**, 951 (1972).
- ⁹D. Biskamp, "Collisionless shock waves in plasmas," *Nuclear Fusion* **13**, 719 (1973).
- ¹⁰B. B. Kadomtsev, *Plasma Turbulence* (Academic Press, 1965).
- ¹¹C. T. Dum, "Anomalous electron transport equations for ion sound and related turbulent spectra," *The Physics of Fluids* **21**, 956–969 (1978).
- ¹²W. Horton, "Ion acoustic turbulence and anomalous transport," *Journal of Statistical Physics* **39**, 739–754 (1985).
- ¹³V. Y. Bychenkov, V. P. Silin, and S. A. Uryupin, "Ion-acoustic turbulence and anomalous transport," *Physics Reports* **164**, 119–215 (1988).
- ¹⁴I. G. Mikellides, I. Katz, D. M. Goebel, and K. K. Jameson, "Evidence of nonclassical plasma transport in hollow cathodes for electric propulsion," *Journal of Applied Physics* **101**, 063301 (2007).
- ¹⁵B. A. Jorns, I. G. Mikellides, and D. M. Goebel, "Ion acoustic turbulence in a 100-a lab 6 hollow cathode," *Physical Review E* **90**, 063106 (2014).
- ¹⁶B. Jorns, A. Lopez Ortega, and I. G. Mikellides, "First-principles modelling of the iat-driven anomalous resistivity in hollow cathode discharges i: Theory," in *52nd AIAA/SAE/ASEE Joint Propulsion Conference* (2016) p. 4626.
- ¹⁷A. Lopez Ortega, I. G. Mikellides, and B. Jorns, "First-principles modelling of the iat-driven anomalous resistivity in hollow cathode discharges ii: Numerical simulations and comparison with measurements," in *52nd AIAA/SAE/ASEE Joint Propulsion Conference* (2016) p. 4627.
- ¹⁸B. A. Jorns, C. Dodson, D. M. Goebel, and R. Wirz, "Propagation of ion acoustic wave energy in the plume of a high-current lab6 hollow cathode," *Phys. Rev. E* **96**, 023208 (2017).
- ¹⁹M. P. Georgin, B. A. Jorns, and A. D. Gallimore, "Correlation of ion acoustic turbulence with self-organization in a low-temperature plasma," *Physics of Plasmas* **26**, 082308 (2019).
- ²⁰M. P. Georgin, B. A. Jorns, and A. D. Gallimore, "Transient non-classical transport in the hollow cathode plume i: measurements of time-varying electron collision frequency," *Plasma Sources Science and Technology* **29**, 105010 (2020).
- ²¹M. P. Georgin and B. A. Jorns, "Transient non-classical transport in the hollow cathode plume ii: evaluation of models for the anomalous collision frequency," *Plasma Sources Science and Technology* **29**, 105011 (2020).
- ²²A. Lopez Ortega and I. G. Mikellides, "The importance of the cathode plume and its interactions with the ion beam in numerical simulations of Hall thrusters," *Physics of Plasmas* **23**, 043515 (2016).
- ²³S. Tsikata, N. Lemoine, V. Pisarev, and D. Grésillon, "Dispersion relations of electron density fluctuations in a Hall thruster, observed by collective light scattering," *Phys. Plasmas* **16**, 033506 (2009).
- ²⁴J. Cavalier, N. Lemoine, G. Bonhomme, S. Tsikata, C. Honoré, and D. Grésillon, "Hall thruster plasma fluctuations identified as the $E \times B$ electron drift instability: Modeling and fitting on experimental data," *Physics of Plasmas* **20**, 082107 (2013).
- ²⁵S. Tsikata, J. Cavalier, A. Héron, C. Honoré, N. Lemoine, D. Grésillon, and D. Coulette, "An axially propagating two-stream instability in the Hall thruster plasma," *Physics of Plasmas* **21**, 072116 (2014).
- ²⁶J.-C. Adam, A. Héron, and G. Laval, "Study of stationary plasma thrusters using two-dimensional fully kinetic simulations," *Phys. Plasmas* **11**, 295 (2004).
- ²⁷K. Hara and S. Tsikata, "Cross-field electron diffusion due to the coupling of drift-driven microinstabilities," *Physical Review E* **102**, 023202 (2020).
- ²⁸S. P. Gary and J. J. Sanderson, "Longitudinal waves in a perpendicular collisionless plasma shock: I. cold ions," *Journal of Plasma Physics* **4**, 739–751 (1970).
- ²⁹R. W. Fredricks, G. M. Crook, C. F. Kennel, I. M. Green, F. L. Scarf, P. J. Coleman, and C. T. Russell, "Ogo 5 observations of electrostatic turbulence in bow shock magnetic structures," *Journal of Geophysical Research* **75**, 3751–3768 (1970).
- ³⁰A. L. Peratt, R. L. Watterson, and H. Derfler, "Coherent scattering of co2 light from ion-acoustic waves," *The Physics of Fluids* **20**, 1900–1910 (1977).
- ³¹R. E. Slusher and C. M. Surko, "Study of density fluctuations in plasmas by small-angle co2 laser scattering," *The Physics of Fluids* **23**, 472–490 (1980).
- ³²B. F. M. Pots, J. J. H. Coumans, and D. C. Schram, "Collective scattering of co2-laser light from ion-acoustic turbulence," *The Physics of Fluids* **24**, 517–527 (1981).
- ³³S. J. Hall, T. G. Gray, J. T. Yim, M. Choi, M. M. Mooney, T. R. Sarver-Verhey, and H. Kamhawi, "The effect of a Hall thruster-like magnetic field on operation of a 25-a class hollow cathode," in *36th International Electric Propulsion Conference* (2019) pp. 1–24.
- ³⁴S. J. Hall, T. G. Gray, J. T. Yim, M. Choi, M. M. Mooney, T. R. Sarver-Verhey, and H. Kamhawi, "The effect of anode position on operation of a 25-a class hollow cathode," in *International Electric Propulsion Conference*, GRC-E-DAA-TN72893 (2019).
- ³⁵G.-C. Potrivitu, S. Mazouffre, L. Grimaud, and R. Jousset, "Anode geometry influence on lab6 cathode discharge characteristics," *Physics of Plasmas* **26**, 113506 (2019).
- ³⁶D. M. Goebel and R. M. Watkins, "Compact lanthanum hexaboride hollow cathode," *Review of Scientific Instruments* **81**, 083504 (2010).
- ³⁷"Finite element method magnetics," <https://www.femm.info/wiki/HomePage>, accessed: 2021-08-15.
- ³⁸J.-P. Boeuf and L. Garrigues, "Low frequency oscillations in a stationary plasma thruster," *Journal of Applied Physics* **84**, 3541–3554 (1998).
- ³⁹R. E. Thomas, H. Kamhawi, and G. J. Williams, *High current hollow cathode plasma plume measurements* (National Aeronautics and Space Administration, Glenn Research Center, 2014).
- ⁴⁰M. P. Bhuva, S. K. Karkari, and S. Kumar, "Characteristics of an elongated plasma column produced by magnetically coupled hollow cathode plasma source," *Physics of Plasmas* **25**, 033509 (2018).
- ⁴¹G. Becatti, D. M. Goebel, and M. Zuin, "Observation of rotating magnetohydrodynamic modes in the plume of a high-current hollow cathode," *Journal of Applied Physics* **129**, 033304 (2021).
- ⁴²I. G. Mikellides, P. Guerrero, A. L. Ortega, D. M. Goebel, and J. E. Polk, "Investigations of spot-to-plume mode transition in a hollow cathode discharge using 2-d axisymmetric plasma simulations, in proceedings of the aiaa," in *SAE/ASEE Joint Propulsion Conference* (2018).
- ⁴³D. H. Froula, S. H. Glenzer, J. N. C. Luhmann, and J. Sheffield, *Plasma Scattering of Electromagnetic Radiation: Theory and Measurement Techniques* (Elsevier, 2011).
- ⁴⁴N. Peacock, D. Robinson, M. Forrest, P. Wilcock, and V. Sannikov, "Measurement of the electron temperature by thomson scattering in tokamak t3," *Nature* **224**, 488–490 (1969).
- ⁴⁵D. Grésillon, C. Stern, A. Hémon, A. Truc, T. Lehner, J. Olivain, A. Quémeneur, F. Gervais, and Y. Lapiere, "Density fluctuation measurement by far infrared light scattering," *Physica Scripta* **1982**, 459 (1982).
- ⁴⁶E. Mazzucato, "Spectrum of small-scale density fluctuations in tokamaks," *Phys. Rev. Lett.* **48**, 1828 (1982).
- ⁴⁷P. Hennequin, R. Sabot, C. Honoré, G. Hoang, X. Garbet, A. Truc, C. Fenzi, and A. Quémeneur, "Scaling laws of density fluctuations at high-k on tore supra," *Plasma Phys. Control. Fusion* **46**, B121 (2004).
- ⁴⁸P. C. Liewer, "Measurements of microturbulence in tokamaks and comparisons with theories of turbulence and anomalous transport," *Nuclear Fusion* **25**, 543 (1985).
- ⁴⁹W. Kasperek and E. Holzhauer, "Co2-laser scattering from thermal fluctuations in a plasma with two ion components," *Physical Review A* **27**, 1737 (1983).
- ⁵⁰E. Holzhauer and J. H. Massig, "An analysis of optical mixing in plasma scattering experiments," *Plasma Physics* **20**, 867 (1978).
- ⁵¹D. M. Goebel, K. K. Jameson, I. Katz, and I. G. Mikellides, "Potential fluctuations and energetic ion production in hollow cathode discharges," *Physics of Plasmas* **14**, 103508 (2007).
- ⁵²T. E. Stringer, "Electrostatic instabilities in current-carrying and counterstreaming plasmas," *Journal of Nuclear Energy. Part C, Plasma Physics*,

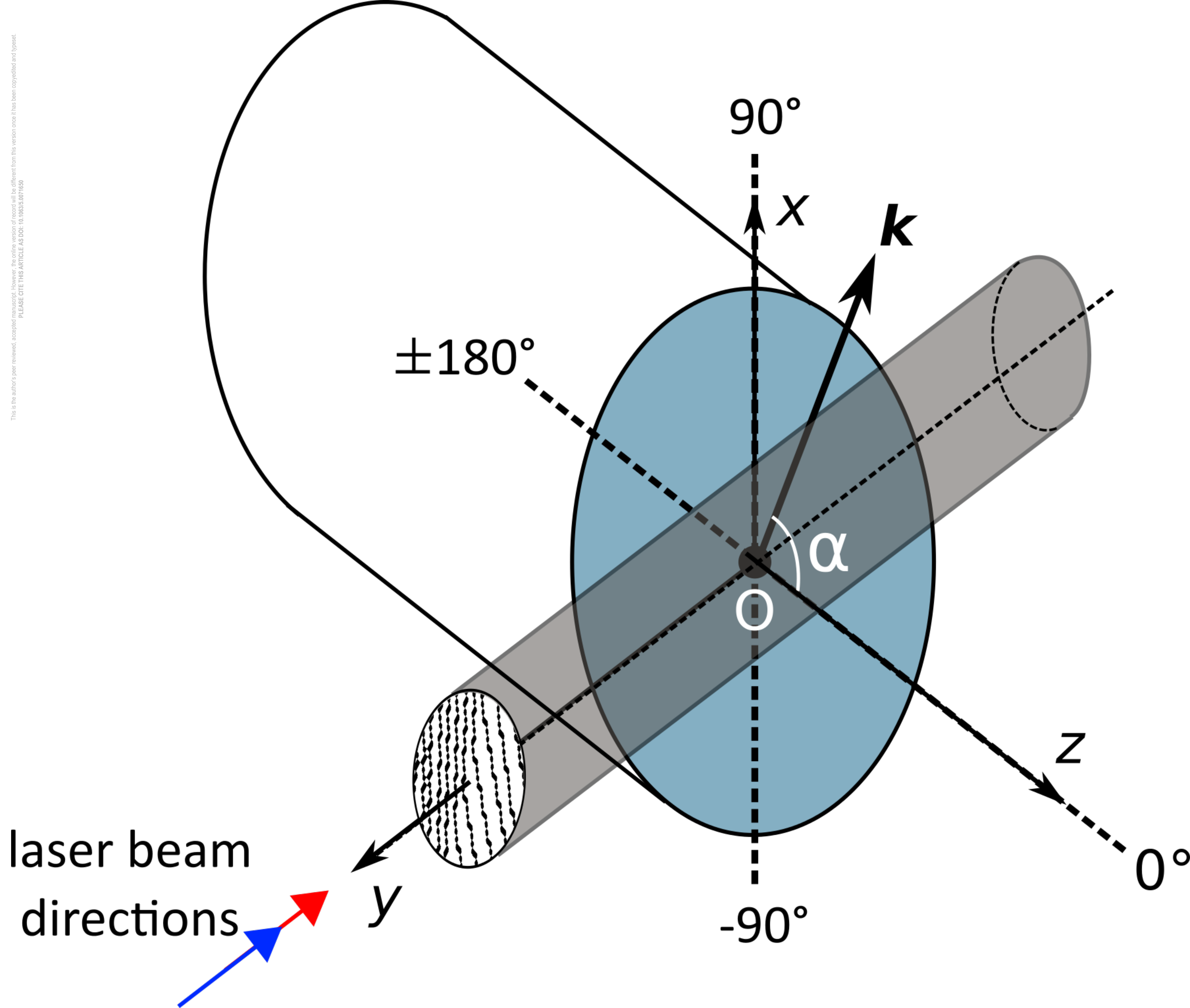
This is the author's peer reviewed, accepted manuscript. However, the online version of record will be different from this version once it has been copyedited and typeset.

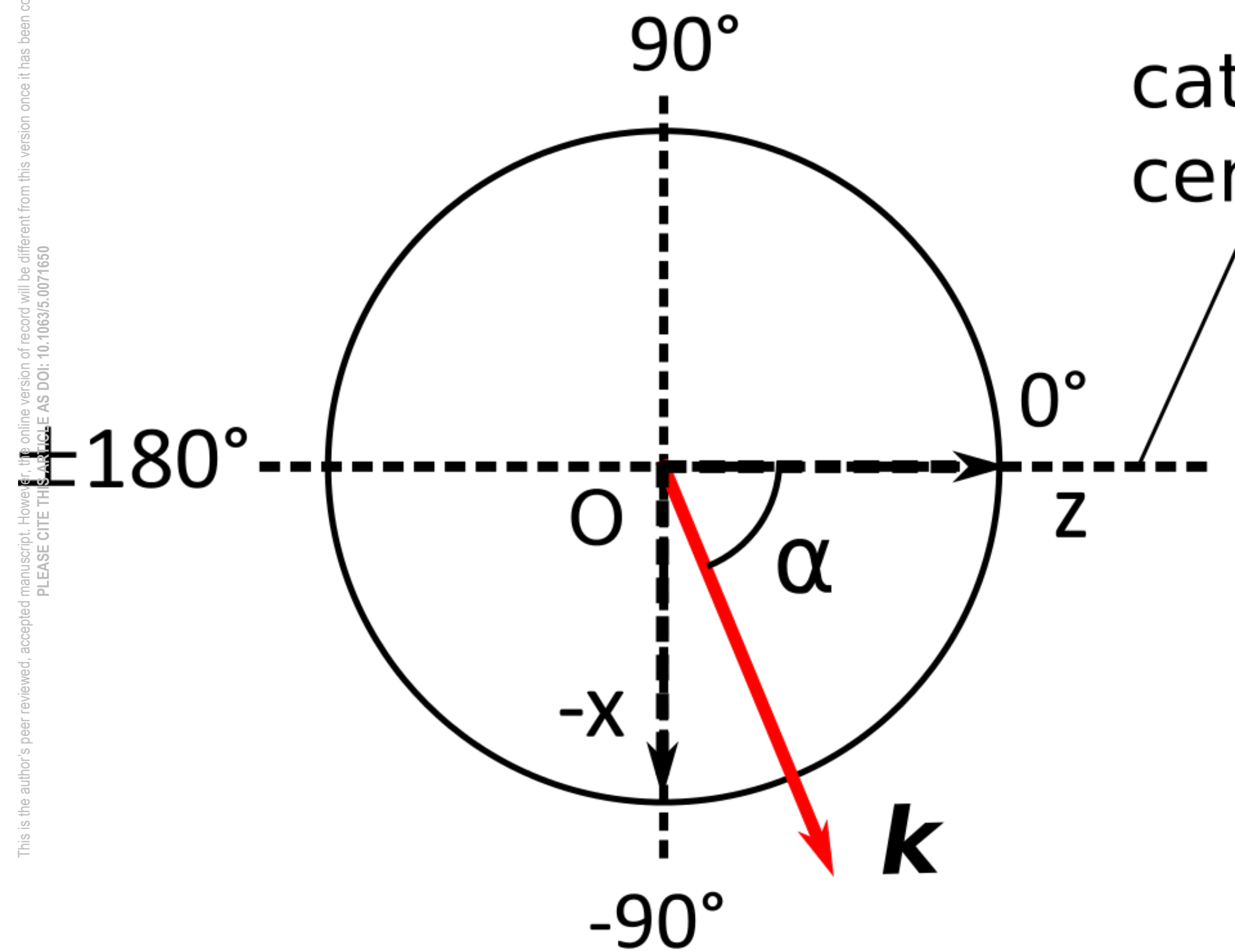
PLEASE CITE THIS ARTICLE AS DOI: 10.1063/5.0071650

- Accelerators, *Thermonuclear Research* **6**, 267–279 (1964).
- ⁵³O. Buneman, “Instability, turbulence, and conductivity in current-carrying plasma,” *Phys. Rev. Lett.* **1**, 8–9 (1958).
- ⁵⁴I. G. Mikellides, I. Katz, D. M. Goebel, K. K. Jameson, and J. E. Polk, “Wear mechanisms in electron sources for ion propulsion, ii: Discharge hollow cathode,” *Journal of Propulsion and Power* **24**, 866–879 (2008).
- ⁵⁵K. Hara and C. Treece, “Ion kinetics and nonlinear saturation of current-driven instabilities relevant to hollow cathode plasmas,” *Plasma Sources Science and Technology* **28**, 055013 (2019).
- ⁵⁶B. A. Jorns and R. R. Hofer, “Plasma oscillations in a 6-kw magnetically shielded Hall thruster,” *Physics of Plasmas* **21**, 053512 (2014).
- ⁵⁷I. M. DesJardin, K. Hara, and S. Tsikata, “Self-organized standing waves generated by ac-driven electron cyclotron drift instabilities,” *Applied Physics Letters* **115**, 234103 (2019), <https://doi.org/10.1063/1.5131019>.
- ⁵⁸R. Kawashima, K. Hara, and K. Komurasaki, “Numerical analysis of azimuthal rotating spokes in a crossed-field discharge plasma,” *Plasma Sources Science and Technology* **27**, 035010 (2018).
- ⁵⁹J.-P. Boeuf and M. Takahashi, “Rotating spokes, ionization instability, and electron vortices in partially magnetized $\mathbf{e} \times \mathbf{b}$ plasmas,” *Physical Review Letters* **124**, 185005 (2020).
- ⁶⁰A. T. Powis, J. A. Carlsson, I. D. Kaganovich, Y. Raitses, and A. Smolyakov, “Scaling of spoke rotation frequency within a penning discharge,” *Physics of Plasmas* **25**, 072110 (2018).
- ⁶¹A. Smolyakov, O. Chapurin, W. Frias, O. Koshkarov, I. Romadanov, T. Tang, M. Umansky, Y. Raitses, I. D. Kaganovich, and V. P. Lakhin, “Fluid theory and simulations of instabilities, turbulent transport and coherent structures in partially-magnetized plasmas of eb discharges,” *Plasma Physics and Controlled Fusion* **59**, 014041 (2016).
- ⁶²I. G. Mikellides and A. Lopez Ortega, “Growth of the lower hybrid drift instability in the plume of a magnetically shielded hall thruster,” *Journal of Applied Physics* **129**, 193301 (2021).
- ⁶³A. Bret, “Weibel, Two-Stream, Filamentation, Oblique, Bell, Buneman...Which one grows faster?” *The Astrophysical Journal* **699**, 990–1003 (2009).
- ⁶⁴J. A. Walker, J. D. Frieman, M. L. R. Walker, V. Khayms, D. King, and P. Y. Peterson, “Electrical facility effects on hall-effect-thruster cathode coupling: discharge oscillations and facility coupling,” *Journal of Propulsion and Power* **32**, 844–855 (2016).
- ⁶⁵B. Vincent, S. Tsikata, G.-C. Potrivitu, L. Garrigues, G. Sary, and S. Mazouffre, “Electron properties of an emissive cathode: analysis with incoherent thomson scattering, fluid simulations and langmuir probe measurements,” *Journal of Physics D: Applied Physics* **53**, 415202 (2020).
- ⁶⁶C. C. Daughney, L. S. Holmes, and J. W. M. Paul, “Measurement of spectrum of turbulence within a collisionless shock by collective scattering of light,” *Physical Review Letters* **25**, 497 (1970).
- ⁶⁷K. Nishikawa and C.-S. Wu, “Effect of electron trapping on the ion-wave instability,” *Physical Review Letters* **23**, 1020 (1969).
- ⁶⁸M. Yamada and M. Raether, “Evolution of the ion- acoustic instability in a direct- current discharge plasma,” *The Physics of Fluids* **18**, 361–368 (1975).
- ⁶⁹S. T. Hepner, E. Tang, E. T. Dale, and B. A. Jorns, “Rotational waves in the plume of an externally-mounted Hall thruster cathode,” *AIAA Journal*, 1–5 (2021).
- ⁷⁰D. B. Ilić, “Spectra of ion acoustic plasma instability,” *The Physics of Fluids* **20**, 1717–1727 (1977).
- ⁷¹R. E. Slusher, C. M. Surko, D. R. Moler, and M. Porkolab, “Study of the current-driven ion-acoustic instability using c o 2-laser scattering,” *Physical Review Letters* **36**, 674 (1976).
- ⁷²A. M. Sleeper, J. Weinstock, and B. Bezzerides, “Nonlinear theory and angular spectrum of the ion-acoustic instability,” *The Physics of Fluids* **16**, 1508–1518 (1973).
- ⁷³A. Hirose, I. Alexeff, and W. D. Jones, “Landau damping of ion acoustic waves in a uniform magnetic field,” *The Physics of Fluids* **13**, 1290–1297 (1970).
- ⁷⁴W. M. Manheimer and R. Flynn, “Anomalous resistivity and ion-acoustic turbulence,” *Physical Review Letters* **27**, 1175 (1971).

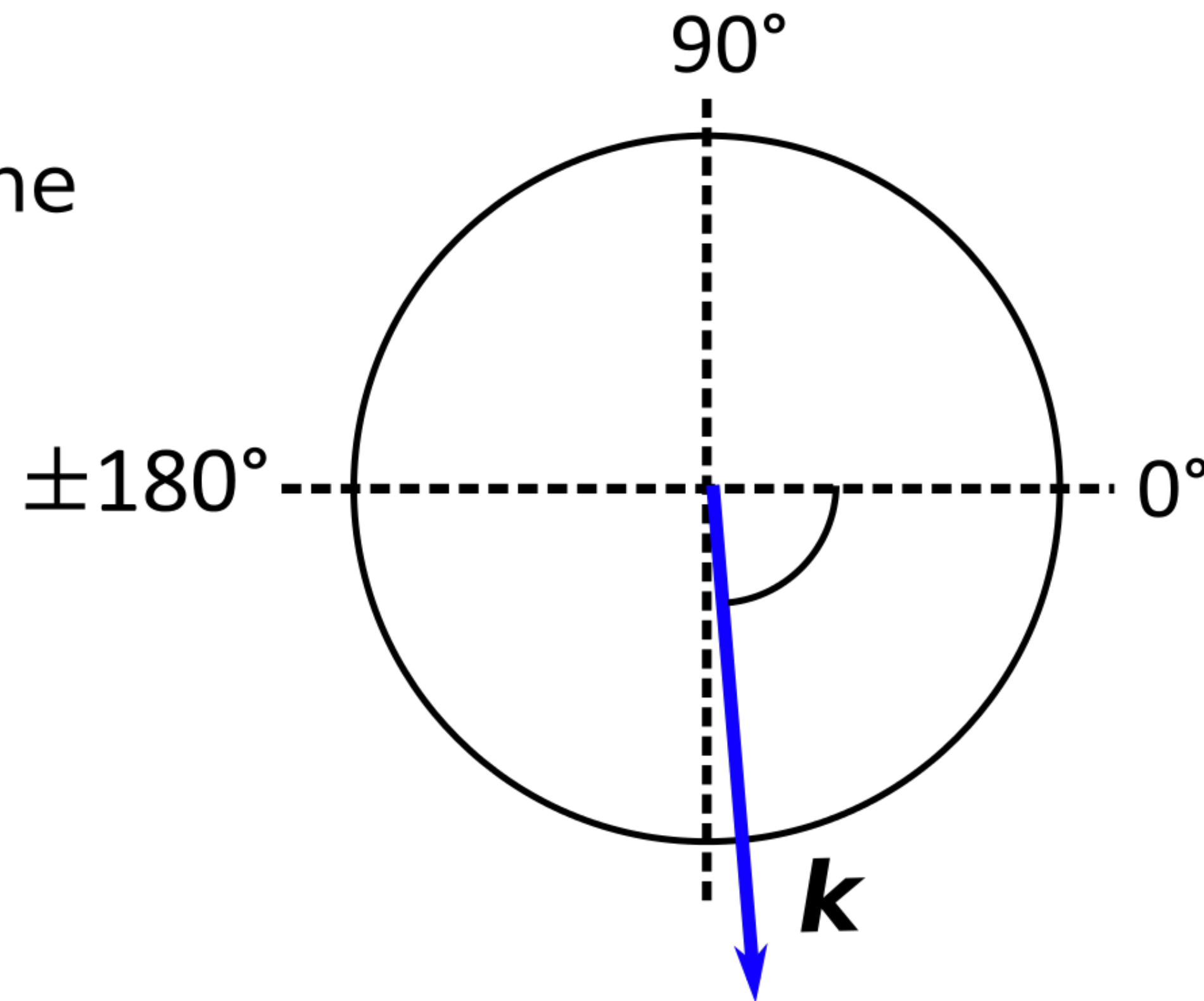




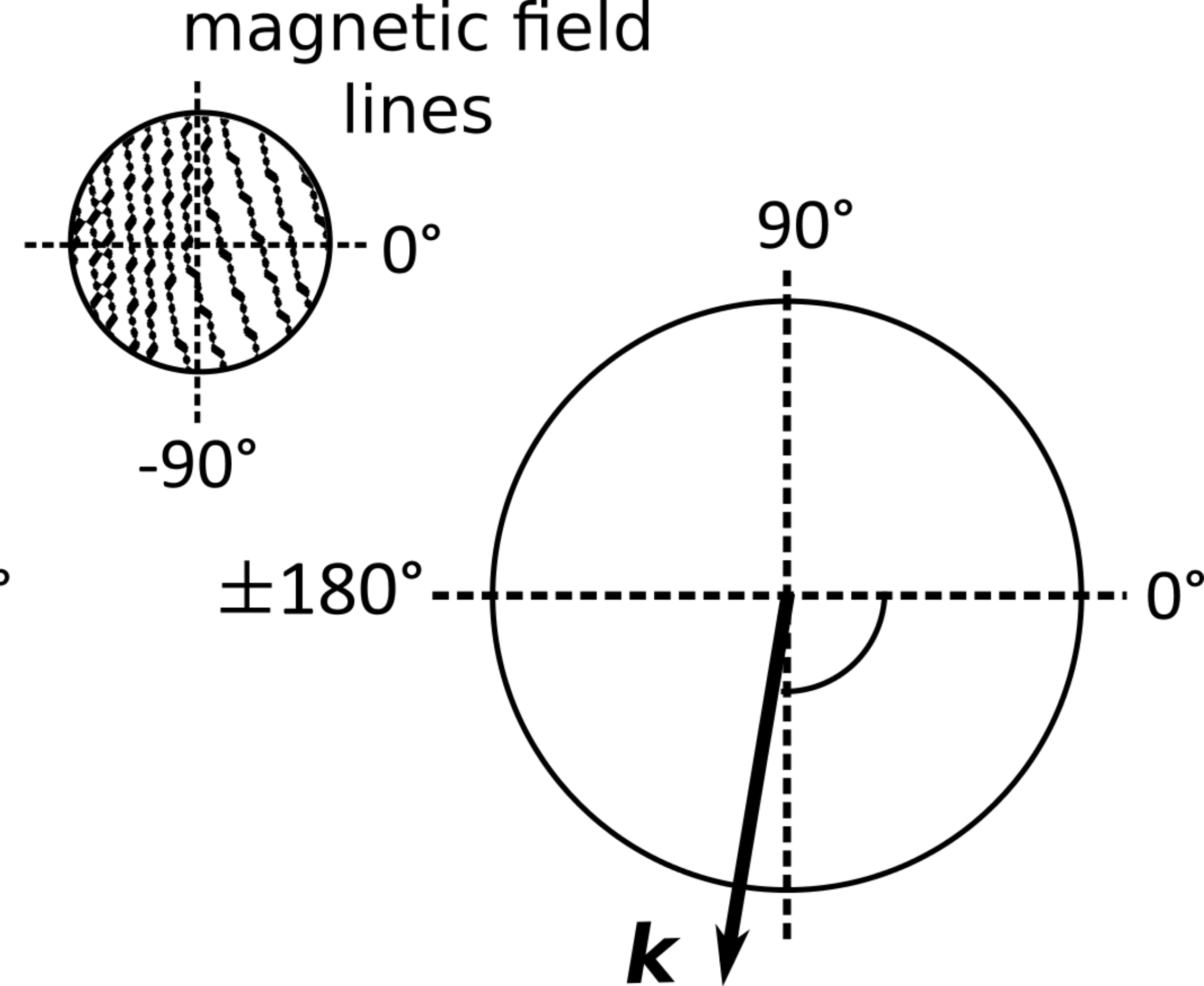




(a) $\alpha = -65^\circ$



(b) $\alpha = -83^\circ$



(c) $\alpha = -110^\circ$

